



VRIJE  
UNIVERSITEIT  
BRUSSEL



Dissertation for the Degree  
Master in Physics and Astronomy

# MULTI-MESSENGER STUDY OF GAMMA-RAY BURSTS

Zeb Van Ranst

Academic year 2019-2020

Promotor: Prof. Dr. Nick Van Eijndhoven  
Co-promotor: Paul Coppin

**sciences and bio-engineering sciences**

This master's thesis came about (in part) during the period in which higher education was subjected to a lockdown and protective measures to prevent the spread of the COVID-19 virus. The process of formatting, data collection, the research method and/or other scientific work the thesis involved could therefore not always be carried out in the usual manner. The reader should bear this context in mind when reading this Master's thesis, and also in the event that some conclusions are taken on board.

## Acknowledgements

A thesis is never a one-man job, so I would like to thank everyone who contributed, directly or indirectly, and made it possible to present this final product.

First of all I would like to thank my parents and grandparents, who have always supported me during my studies and never doubted me, even when they should have. Throughout my life, they were the ones who continuously and repeatedly guided me when making the choices that made me the person that I am today.

I would also like to express my more than everlasting gratitude towards my promotors Nick and Paul, who provided me with the expertise and know-how on the subject that allowed me to complete this thesis. They always took the time to listen to my questions and answer them elaborately. It has been a privilege to discuss physics with both of these fine gentlemen. The VUB is lucky to have you!

Next, I want to sincerely thank all my classmates, especially Yens, Dieder and Sander. I am so glad that our choices and common interests have set us up for this wonderful ride. Things haven't always been easy while doing these studies, but I feel like these hard times in particular made us grow closer to each other. The moments we shared together in the office were absolutely priceless and they will live in my memories forever. I wish you guys all the best in making your dreams come true, where ever they may lead you.

Of course I can't forget the entirety of the Gravitational Wave and Fundamental Physics group at Maastricht University, where I have been accepted to do an internship. I have had the most wonderful time there as I got to experience what it is like to be part of a research group. They also taught me a thing or two about interferometers, which has been incredibly helpful for writing this thesis. It is truly a marvelous place with brilliant people in every way. Andrei, Annabel, Gideon, Stefan, the other Stefan, Viola, Ayatri, Sebastian, Jessica - I wish you all the best.

Although I don't know him personally, I would like to thank Ruben De Smet, who provided the LaTeX template for this, and probably many other theses. Also the IT team of the IIHE deserves special thanks for granting me access to their servers, enabling me to carry out the calculations needed to complete the thesis.

Finally, I would like to thank Stijn Buitink and Freya Blekman, who have accepted to read this thesis as part of the reading committee. While we're at it, I would like to thank them for their engaging lectures and/or lab sessions as well.

### **Abstract**

Gamma-Ray Bursts (GRBs) are among the most violent events in the universe and promising subjects for multi-messenger studies. Not only do they release electromagnetic radiation at all wavelengths, they are also thought to be the source of at least some part of the high-energy cosmic-ray and neutrino spectrum. Recently, the gravitational wave event GW 170817 of a Binary Neutron Star (BNS) merger has been linked to the short gamma-ray burst GRB 170817A, confirming that some GRBs can be studied through gravitational waves as well. Such events are expected to be observed at a staggering rate of  $7 \times 10^4 \text{ yr}^{-1}$  by the future Einstein Telescope (ET), a next-generation gravitational wave detector. In this thesis, a toy model will be used to estimate the operation time needed to detect an observable neutrino excess from short-duration GRBs by IceCube, based on the BNS merger rate of ET and the current limits on the GRB neutrino flux.

# Contents

<b>1</b>	<b>Gamma-ray bursts</b>	<b>5</b>
1.1	Electromagnetic observations . . . . .	5
1.2	Progenitors . . . . .	7
1.3	The fireball model . . . . .	7
1.3.1	The compactness problem . . . . .	8
1.3.2	Neutrino production . . . . .	11
<b>2</b>	<b>Connection with gravitational waves</b>	<b>14</b>
2.1	Importance for multi-messenger astronomy . . . . .	14
2.2	Gravitational wave detection . . . . .	14
2.3	Third-generation interferometers . . . . .	17
2.3.1	Einstein Telescope . . . . .	17
2.3.2	Cosmic Explorer . . . . .	19
<b>3</b>	<b>Neutrino detection with IceCube</b>	<b>20</b>
3.1	The IceCube detector . . . . .	20
3.2	Neutrino cross sections . . . . .	21
3.3	Event selection . . . . .	21
3.4	The astrophysical neutrino spectrum . . . . .	23
3.5	Simulating neutrino interactions . . . . .	24
3.6	Detector sensitivity . . . . .	26
<b>4</b>	<b>NcAstrolab toy model</b>	<b>30</b>
4.1	Time profile stacking . . . . .	30
4.2	Bayesian logical interference . . . . .	31
<b>5</b>	<b>Results of the Toy model</b>	<b>34</b>
5.1	Model parameters . . . . .	34
5.2	Interpretation of results . . . . .	35
<b>6</b>	<b>Conclusion and outlook</b>	<b>39</b>

# 1 Gamma-ray bursts

## 1.1 Electromagnetic observations

Gamma-Ray Bursts (GRBs) have been among the most mysterious phenomena in the astronomical scene since their discovery in 1967 by the Vela 3 & 4 satellites [1]. These military satellites were originally developed and launched by the US to detect nuclear tests that would violate the Nuclear Test Ban Treaty signed by the US, the UK and the USSR. The on-board gamma-ray scintillators of these satellites and their successors confirmed the regular occurrence of gamma-ray flashes. It soon became clear that the flashes were not caused by nuclear weapons or any terrestrial phenomena [2]. Besides this, not much was known about the origin of these flashes or the mechanisms involved. One of the most urgent questions that had to be answered was at which distance scales the GRBs happened. This could be anywhere from the outer regions of our solar system up to cosmological distances. Uncovering the distance scales would give an idea of the amount of energy radiated by GRBs and the physics required to produce them. Assuming that a GRB source at distance  $r$  emits radiation isotropically, the total energy  $E$  emitted during the burst is given by

$$E = 4\pi r^2 S, \quad (1)$$

where  $S$  is the total observed energy per unit of detector area, called the energy fluence. In the 10-1000 keV range the fluence of bursts typically varies from  $10^{-7}$  to  $10^{-4}$  erg/cm<sup>2</sup> [3]. For a GRB with a fluence of  $10^{-5}$  erg/cm<sup>2</sup> at a distance of 50 000 Astronomical Units (AU) in the Oort cloud, the corresponding energy of the burst is  $7 \times 10^{31}$  erg. This is already comparable to the total amount of energy radiated onto the earth's surface during one year. If instead a burst with the same fluence is located in a galaxy 1 Gpc away, the total energy would be  $10^{51}$  erg. This is close to the energy output during the *entire* lifetime of the sun, or about  $10^{-3} M_{\odot} c^2$ .

The first strong hint that GRBs were of extragalactic origin came with the launch of the Compton Gamma Ray Observatory (CGRO) in 1991 [4]. On board was the Burst And Transient Source Experiment (BATSE), which was sensitive to gamma radiation in the 15 keV to 110 MeV energy range [5]. The observatory was able to detect over 2700 GRBs with an angular accuracy of a few degrees over a period of 9 years. The resulting angular distribution of GRBs appeared to be isotropic, disfavouring a galactic origin [6]. However, it was still possible that GRBs were only visible within the stellar neighbourhood where an isotropic distribution would be expected. Conclusive evidence that GRBs are extragalactic was provided by the Italian-Dutch satellite BeppoSAX (launched in 1996), which could determine the positions of GRB afterglows up to arcminute accuracy [7]. These areas were small enough to effectively search for afterglows in the X-ray and/or visible spectrum. The advantage of searching in the X-ray regime is that source positions can be determined more accurately than for  $\gamma$ -rays and that the sky is not very crowded with X-ray sources in comparison to optical sources for example. With this method the error box could be systematically reduced, from the relatively large  $\gamma$ -ray areas to smaller ones for X-rays and finally the ones for visible light which could be less than an arcsecond large. BeppoSAX did in fact find the first GRB afterglow 8 hours after GRB 970228 in the X-ray spectrum, followed by an optical counterpart detected by the William Herschel Telescope [8]. The resolution of this telescope (0.421 arcsec) was sufficient to identify the host galaxy of which the redshift was estimated to be between 0.2 and 2 [9]. The faintness of the galaxy made it difficult to find the exact redshift value. However, not much later the redshift of GRB 970508 was found to be  $z = 0.835$  based on an analysis of the spectral lines, confirming the extragalactic and even cosmological distance scales of GRBs [10]. This meant that these bursts must generate an enormous energy output in a generally small amount of time ranging from milliseconds to seconds. The light curves of different GRBs show a lot of diversity and generally do not exhibit a characteristic burst profile.

Twelve examples of light curves are shown in Figure 1 with features such as one or multiple peaks, an exponential decay or nearly periodic patterns. Some GRBs, like Trigger 2067, show a small precursor phase of gamma-ray emission before the main prompt emission phase.

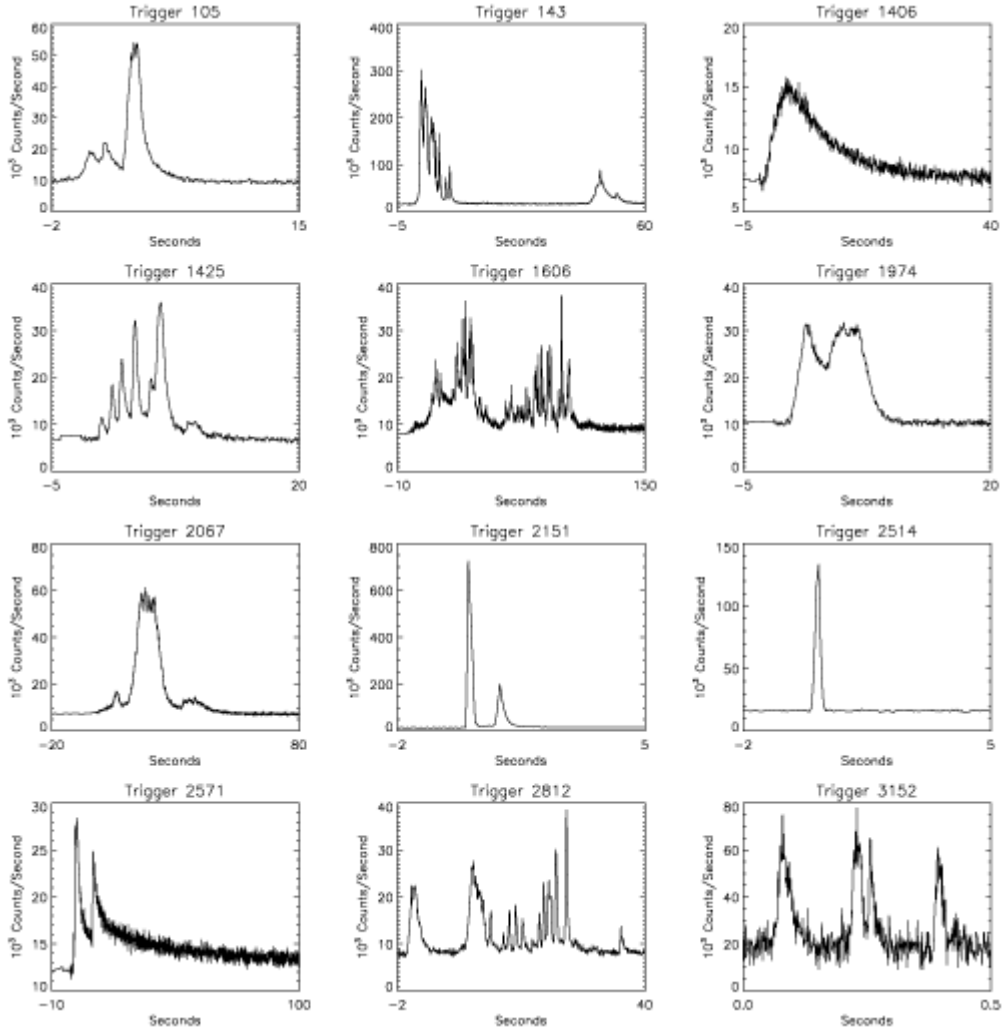


Figure 1: Different types of GRB light curves measured by the Compton Gamma-Ray Observatory. Public domain image by J.T. Bonnell (NASA/GSFC).

The duration of a burst is quantified by  $T_{90}$ , the central time interval during which 90% of the fluence is detected. Based on the distribution of the  $T_{90}$  quantity, all GRBs are separated into two classes: long and short GRBs (see Figure 2). Long GRBs have  $T_{90} > 2$  s and a 30 s average, while short GRBs include everything with  $T_{90} < 2$  s and this population has an average of around 1.05 s [3]. Because of the clear separation between the long and short GRB population, it is most likely that they are powered by different kinds of objects. There is however some overlap between the  $T_{90}$  of both populations, meaning that it would be helpful to obtain additional criteria to classify a GRB as long or short. This could be in the form of a clear identification of the GRB progenitor. Within each category there is also still a lot of variation, with the shortest bursts having a duration of tens of milliseconds and the longest one over 7 hours [11]. It is thought that these ultra-long GRBs with a  $T_{90}$  of several hours could constitute another separate population with different progenitors, thought to be blue supergiants. However, additional multi-wavelength observations are needed to make any definite conclusions [12].

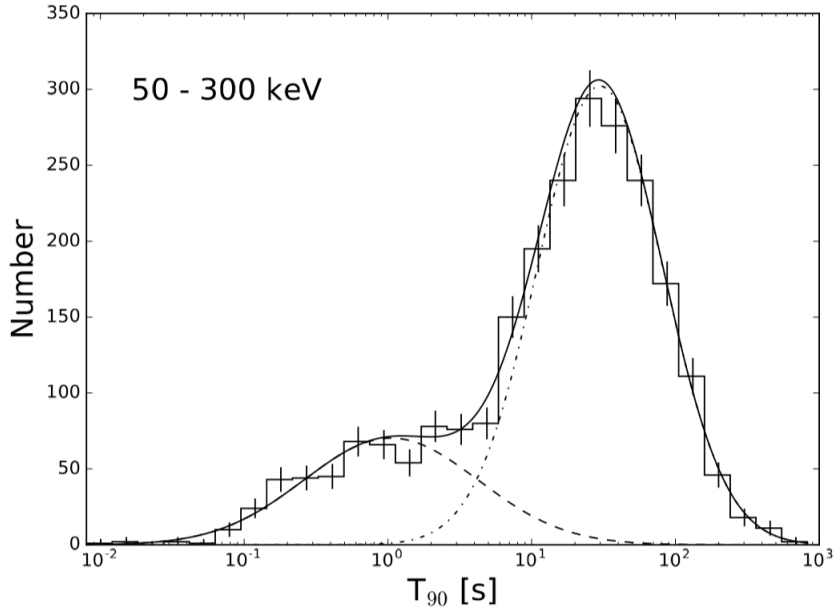


Figure 2:  $T_{90}$  distribution of the first 10 years of the Fermi-GBM mission. The sample contains in total 2353 burst of which 17% are short GRBs and 83% are long GRBs. From von Kienlin (2020) [3].

## 1.2 Progenitors

The classification of long and short GRBs is not merely an arbitrary choice to separate events into two conveniently distinct groups. There is a clear difference in the nature of the host galaxies and consequently also the supposed progenitors of the bursts. Long GRBs (LGRBs) often occur in star-forming regions and are repeatedly associated with the core-collapse of massive, short-lived stars [13]. Short GRBs (SGRBs) on the other hand seem to occur more frequently in regions with low star formation and they are thought to be the result of compact binary mergers consisting of two neutron stars or a neutron star and a black hole [14, 15].

## 1.3 The fireball model

The short-duration variabilities in the light curves of GRBs suggest that they are caused by stellar-sized objects that suddenly release large amounts of energy in the form of radiation and a relativistic matter outflow, like gravitational collapse of a massive star or binary star mergers [16–18]. The fireball model aims to explain the observation of electromagnetic radiation, cosmic rays and neutrinos, without assuming a specific progenitor of the matter outflow. One of the main criteria for the fireball model is that it has to explain the non-thermal spectrum of GRB prompt emission and that it has to lead to an emission source for the afterglow that is subsequently observed.

### 1.3.1 The compactness problem

First of all, note that high-energy photons in the MeV-GeV energy range are being observed in GRBs in significant proportions [19, 20]. The short variations  $\delta t$  in the light curves of GRBs are typically of order 10 ms, see Figure 1. This insinuates that the size of the source is of the order  $c \delta t = 3 \times 10^6$  m. But in a volume so small and with a photon intensity so large, the  $\gamma$ -rays will efficiently produce electron-positron pairs by pair creation ( $2\gamma \rightarrow e^+e^-$ ) [21]. In other words; the outflow is opaque to its own radiation and any photons with energy above  $m_e c^2 = 511$  keV would be suppressed. But according to observation this high-energy radiation can, at least partially, escape the source.

This is called the *compactness problem*. It is resolved by assuming that the flow expands ultra-relativistically. A source expanding with a high Lorentz factor  $\Gamma$  will exhibit relativistic Doppler and timing effects with respect to a detector in the lab frame at Earth [22]. First of all, incorporating the Doppler effect means that the wavelengths of  $\gamma$ -ray photons in the lab frame will be shortened compared to the comoving frame. So the observed photons have a lower energy in the comoving frame of the outflow after performing a Doppler shift. For high enough  $\Gamma$ , the photon energy in the comoving frame can drop below the energy threshold of  $m_e c^2$  such that pair creation does not take place. The energy condition for two photons with comoving frame energies  $E'_1$  and  $E'_2$  to prevent pair creation is

$$E'_1 E'_2 \leq (m_e c^2)^2, \quad (2)$$

for a head-on collision. This sets a requirement for the Lorentz factor  $\Gamma$  after replacing the comoving frame energies by their Doppler-boosted equivalents  $E_{1,2} = E'_{1,2} \Gamma$  in the lab frame

$$E_1 E_2 \leq \Gamma^2 (m_e c^2)^2. \quad (3)$$

In addition, the observed time variations  $\delta t_o$  are altered by relativistic timing effects because of the motion of the source, which in this case is an expanding shell of matter. To remain general, it can be assumed that the flow expands along an axis tilted with respect to our line of sight under an angle  $\theta$ , and that it sends out two signals a time  $\delta t$  apart, as shown in Figure 3. The two signals will arrive to the observer a time  $\delta t_o = (1 - \beta \cos \theta) \delta t$  apart, due to the fact that the outflow will trail its own emitted radiation. If the flow is indeed highly relativistic ( $\Gamma \gg 1$ ) then the velocity fraction  $\beta$  can be well approximated by

$$\beta = \sqrt{1 - \frac{1}{\Gamma^2}} \approx 1 - \frac{1}{2\Gamma^2}. \quad (4)$$

The observed time difference along the line of sight of the observer ( $\theta = 0$ ) is then

$$\delta t_o = \frac{\delta t}{2\Gamma^2}. \quad (5)$$

Due to this timing effect, the actual size of the source is of the order

$$D = c \delta t = 2c \Gamma^2 \delta t_o = (6 \times 10^6 \text{ m}) \Gamma^2. \quad (6)$$

For high enough  $\Gamma$ , the physical size of the source can be large enough to avoid photon loss by pair creation. The required Lorentz factor is found by relating the optical depth  $\tau_{\gamma\gamma}$  of the relativistic outflow to the size of the source.

The optical depth can be approximated as

$$\tau_{\gamma\gamma} = \sigma_T n_\gamma D = \frac{D}{\lambda}, \quad (7)$$

with  $n_\gamma$  the number density of photons in a GRB,  $D$  the size of the source and  $\lambda$  the mean free path of the photons [22]. The Thomson cross-section  $\sigma_T$  approximates the pair creation cross section well when the photon energy is close to the electron rest mass [23]. Let us assume again a typical burst with a fluence  $S = 10^{-5}$  erg/cm<sup>2</sup> at a luminosity distance of 1 Gpc, implying a total isotropic energy output of  $E = 10^{51}$  erg. The photon number density for a spherical emission region with radius  $D$  is

$$n_\gamma = \frac{3}{4\pi D^3} f \frac{E}{\epsilon_\gamma}, \quad (8)$$

with  $\epsilon_\gamma = \Gamma^2 m_e c^2$  the threshold energy imposed by pair creation (in the lab frame) and  $f$  the fraction of photons that exceed this threshold. Combining Equations (6) and (8) with Equation (7) gives the optical depth

$$\tau_{\gamma\gamma} = \frac{3\sigma_T f E}{4\pi D^2 \epsilon_\gamma} = 5.4 \times 10^{14} \frac{f}{\Gamma^6}. \quad (9)$$

The fraction  $f$  depends on the burst and the detector used to measure the photon count in a certain energy range, but is typically of order unity. In order to solve the compactness problem the optical depth should be below unity. This can be achieved by a high Lorentz factor  $\Gamma > 285$  for  $f = 1$  or  $\Gamma > 194$  if  $f = 0.1$ , all for this specific burst. The dependence on  $\Gamma$  in Equation (9) varies with the underlying photon spectrum. Here a spectral index  $\beta = -2$  is assumed implicitly. Zhang (2019) [22] assumes a Band spectrum with a spectral index  $\beta \simeq -2.2$  (see next section). For this specific photon spectrum, the optical depth scales as  $\Gamma^{-6.4}$  instead.

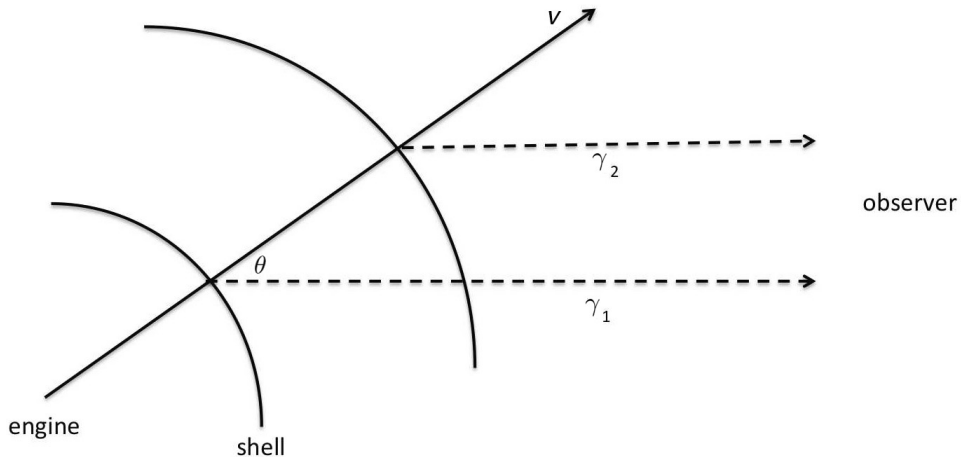


Figure 3: The geometry of an expanding shell with velocity  $v$  emitting two signals  $\gamma_1$  and  $\gamma_2$  a time  $\delta t$  apart. In the case of a GRB that emits isotropically or is beamed towards Earth, the angle  $\theta$  is effectively zero. From Zhang (2019) [22].

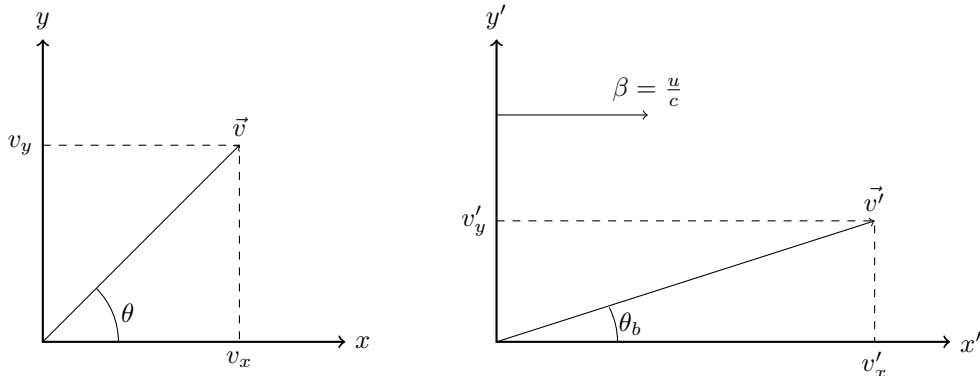


Figure 4: The effect of relativistic aberration. The frame on the left is the fireball rest frame and on the right, the lab frame on Earth is shown, in which the source moves with a relative velocity  $u$  and a Lorentz factor  $\Gamma = (1 - u^2/c^2)^{-1/2}$ .

One crucial consequence for the phenomenology of GRBs is the effect of relativistic aberration. An outflow that moves at high velocities will beam its radiation within a certain angle, as seen from Earth. This can be understood by considering a beam of light, being emitted by the outflow at an angle  $\theta$  in the rest frame of the fireball. In the lab frame on Earth, moving with a relative velocity  $u$ , this angle appears to be smaller and so the emission is beamed. The beam of light has a velocity component  $v_x = c \cos \theta$  along the line of sight of the observer and a component  $v_y = c \sin \theta$  along the perpendicular direction, as shown in Figure 4. When going from one frame to the other, these velocity components transform according to the relativistic velocity addition formula

$$v'_x = \frac{v_x + u}{(1 + v_x u/c^2)} \quad v'_y = \frac{v_y}{\Gamma(1 + v_x u/c^2)}. \quad (10)$$

The beamed angle  $\theta_b$  in the lab frame is defined by

$$\tan \theta_b = \frac{v'_y}{v'_x} = \frac{v_y}{\Gamma(v_x + u)} = \frac{\sin \theta}{\Gamma(\cos \theta + \beta)}. \quad (11)$$

For an ultra-relativistic flow (implying  $\beta \simeq 1$  and  $\Gamma \gg 1$ ) and an opening angle  $\theta = \pi/2$ , the beamed angle becomes

$$\tan \theta_b \simeq \theta_b \simeq \frac{1}{\Gamma}. \quad (12)$$

So it has been shown that a relativistic outflow will beam its emission within a cone with opening angle  $\theta_b \sim 1/\Gamma$ . For an isotropic outflow, one would only observe the emission coming from a spot within an opening angle  $\theta_b$ . However, if the outflow itself expands in a jet with opening angle  $\theta_j$  towards Earth, some very distinctive effects can be observed. As long as the opening angle of the jet is larger than that of the beamed emission ( $\theta_j > \theta_b$ ), there would be no observational difference from isotropic flow. But due to the outflow being slowed down by the surrounding interstellar medium, the beaming angle steadily increases and at one point surpasses the jet angle, as shown in Figure 5. At this point, the luminosity from the source will decrease at a faster rate because now the radiation that would be emitted towards Earth at an angle  $\theta_j$ , is not there. This effect has been observed for a number of GRB afterglows and can be used to constrain the jet opening angle. Most GRBs seem to have a jet opening angle around  $4^\circ$  and, in some cases, angles as large as  $20^\circ$  have been observed [24].

A direct consequence of beamed GRB outflows is that only a fraction  $2\Omega_j/4\pi = 2\sin^2\frac{\theta_j}{2}$  of the total GRB population is aimed towards Earth<sup>1</sup>. This implies that up to 1000 GRBs can take place every day [25].

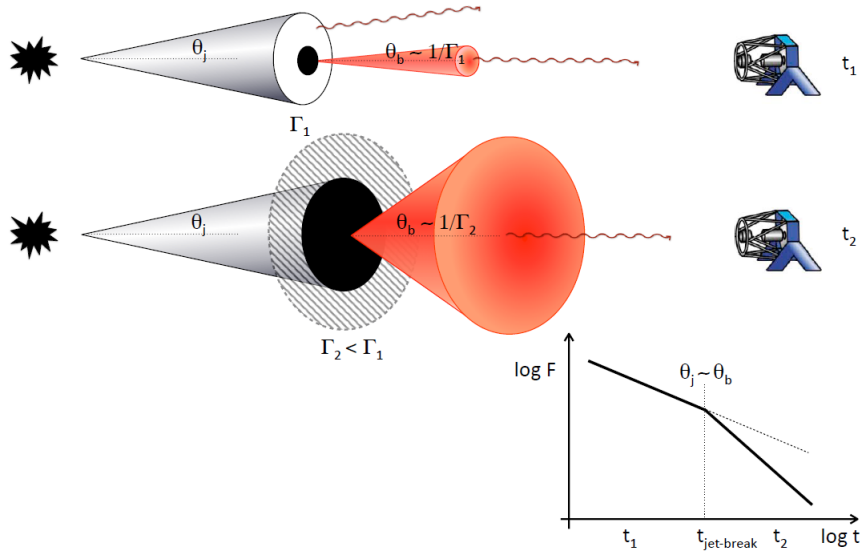


Figure 5: Schematic representation of the break in the light curve of a GRB. The emission from the black area contributes to the observed fluence. When  $\theta_b > \theta_j$  the black area would extend beyond the edges of the jet. From Gomboc (2012) [25].

### 1.3.2 Neutrino production

Neutrinos are known for their ability to traverse large amounts of matter without interacting, which is exactly why they are preferred messengers of information about the physical processes in GRBs. Photons will almost inevitably interact with the surrounding (charged) matter in the outflow and other photons by pair creation, inverse Compton scattering, thermalised emission, etc. Neutrinos on the other hand, once produced, will escape the fireball unharmed long before it becomes transparent to most photons. This means that they will retain their energy given to them when they were produced, preserving the information of the physical process involved. Since they are uncharged, their trajectories are also not altered by the magnetic fields of galaxies, such that they always point at their source.

Protons in a GRB environment can be accelerated to high energies up to  $10^{20}$  eV by the first-order Fermi acceleration mechanism [26]. This is a process where a charged particle is repeatedly accelerated by a shock front. A particle, that is initially ahead of the shock, will eventually be overtaken by the shock front. Behind the shock front, the motion of the particle will become randomised in the frame that is co-moving with the shock front. As a result, the particle can cross the shock front again. This process delivers a net gain of energy to the particle and can be repeated several times before the particle escapes. These shocks can be external, due to the outflow particles colliding with the interstellar medium, or they can be internal, due to instabilities in the outflow. High-energy electrons are expected to be accelerated by the same mechanism, emitting synchrotron radiation with energy  $\sim$ MeV [27]. These synchrotron photons can interact with the protons, producing a  $\Delta^+$  resonance.

<sup>1</sup>The factor 2 arises from the assumption that two back-to-back jets of equal size are produced.

The  $\Delta^+$  baryon quickly decays, most commonly to a proton along with a neutral pion or to a neutron along with a charged pion. Further decay of charged pions finally produces muon- and electron-flavoured neutrinos.

$$p + \gamma \rightarrow \Delta^+ \rightarrow n + \pi^+ \quad (13)$$

$$\pi^+ \rightarrow \mu^+ + \nu_\mu \rightarrow e^+ + \nu_e + \bar{\nu}_\mu + \nu_\mu$$

The center-of-mass energy of the initial photon and proton needs to be sufficiently high to reach the  $\Delta^+$  baryon mass of 1.23 GeV. This sets a threshold energy  $E_t$  for the photon energy  $E_\gamma$  and the proton energy  $E_p$

$$E_p E_\gamma \geq 0.16 \Gamma^2 \text{ GeV}^2 = E_t^2. \quad (14)$$

The  $\Gamma^2$  factor arises after transforming from the comoving frame to the observer frame, similar to how the pair creation energy threshold was being raised in Equation (3). The pions on average obtain 20% of the initial proton energy and assuming that the remaining energy of the muon decay is distributed evenly between the neutrinos, each neutrino carries  $\sim 5\%$  of the proton energy  $E_p$  [27]. For protons with  $E_p \geq 10^{16}$  eV, the  $p\gamma$  interactions can produce neutrinos in the 100 TeV to EeV range [28].

The neutrino spectrum naturally follows the proton spectrum, characterised by a power law with spectral index  $s$  between  $-2.2$  and  $-2.3$ , as is expected for Fermi acceleration [29]. However, a spectral index of  $-2$  is often employed for simplicity. On the other hand, the neutrino spectrum is also proportional to the amount of photons that can interact with the protons through the  $\Delta^+$  resonance. The photon spectrum follows a broken power law spectrum with an exponential cutoff, called the Band function [30]

$$\frac{d\Phi_\gamma}{dE} = N_0 \times \begin{cases} e^{-E/E_0} E^\alpha & \text{for } E < (\alpha - \beta)E_0 \\ [(\alpha - \beta)E_0]^{\alpha - \beta} e^{\beta - \alpha} E^\beta & \text{for } E > (\alpha - \beta)E_0 \end{cases} \quad (15)$$

Although the spectral parameters are not universal for every burst, the low-energy spectral index is clustered around  $\alpha = -1$  and the high-energy spectral index around  $\beta = -2.2$  [31]. The flux of photons available for the  $\Delta^+$  resonance is found by integrating the Band function from the photon energy threshold  $E_t^2/E_p$  up to infinity

$$\Phi_\gamma(E_\gamma > E_t^2/E_p) = \int_{E_t^2/E_p}^{\infty} \frac{d\Phi_\gamma}{dE} dE. \quad (16)$$

When the proton energy is low enough, only the part of the Band function above the energy break will be integrated and  $\Phi_\gamma \sim E_p^{-\beta-1}$ . This is because a proton with a lower energy has to interact with a higher-energy photon to reach the threshold energy. For larger values of  $E_p$ , the part of the Band function that is scaled as  $E^{-\alpha}$  is included such that  $\Phi_\gamma \sim E^{-\alpha-1}$ , in general<sup>2</sup>. In this way, the neutrino spectrum inherits the energy break from the photon spectrum. At very high energies, the charged pions produced by  $\Delta^+$  decay will experience meson cooling. The high-energy pions and muons will lose a significant fraction of their energy before decaying because of synchrotron radiation, introducing an additional proportionality  $E_\nu \sim E_\pi^{-2}$  beyond a second energy break [32].

---

<sup>2</sup>In the case that  $\alpha = -1$ , we implicitly assume that  $\ln(E)$  varies slowly enough to be considered constant.

Including the proportionality from both the proton spectrum and the number of available photons, the resulting neutrino flux follows the Waxman-Bahcall spectrum

$$\frac{d\Phi_\nu}{dE} = \Phi_0(\varepsilon_b) \begin{cases} \varepsilon_b^{-1} E^{s-\beta-1} & \text{for } E < \varepsilon_b \\ E^{s-\alpha-1} & \text{for } \varepsilon_b < E < 10\varepsilon_b, \\ (10\varepsilon_b)^2 E^{s-2} & \text{for } E > 10\varepsilon_b \end{cases} \quad (17)$$

as shown in Figure 6. This is expected to be the neutrino flux produced during a GRB [33]. The spectral shape changes discontinuously at the first energy break  $\varepsilon_b$  and again at the second break for  $E = 10\varepsilon_b$ . Typically, the spectral index of the proton spectrum  $s$  and the high-end Band spectrum  $\beta$  are both taken to be  $-2$ , while the low-end Band spectrum has  $\alpha = -1$ . This leads to a Waxman-Bahcall flux spectrum that starts off with a spectral index of  $-1$ , dropping to  $-2$  after the first break and further decreasing to  $-4$  after the second break.

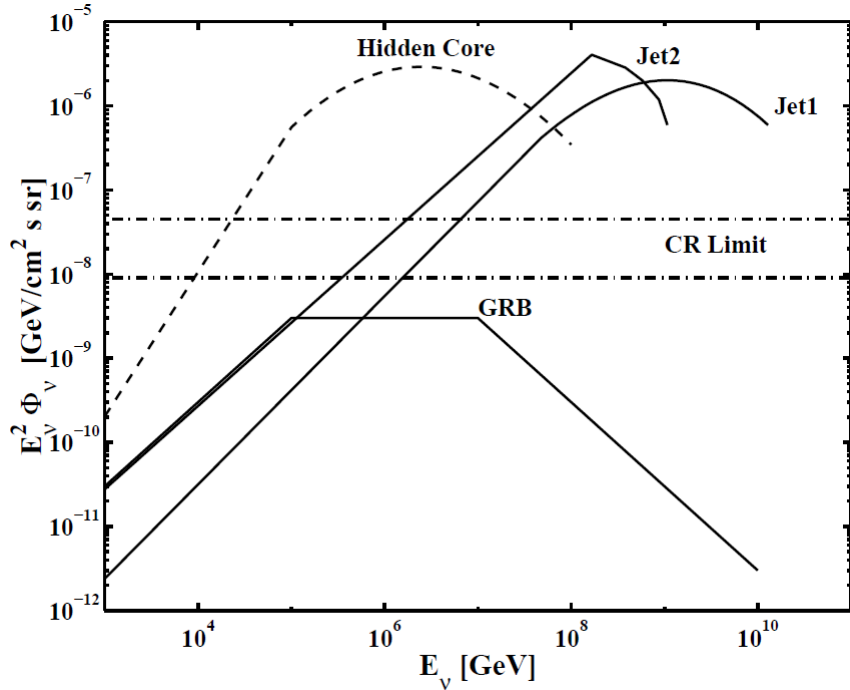


Figure 6: The Waxman-Bahcall flux (labeled by “GRB”) for muon neutrinos compared to Active galactic Nuclei (AGN) jet models and the limits set by the cosmic-ray flux. The hidden core model for AGNs predicts a neutrino flux without a cosmic-ray counterpart, and therefore the CR limit does not apply to it. From Waxman (1998) [34].

## 2 Connection with gravitational waves

### 2.1 Importance for multi-messenger astronomy

The recent advent of gravitational waves (GWs) as a viable detection method proves to be especially useful when it comes to SGRBs. Gravitational waves have been predicted by Einstein over a hundred years ago in 1916, one year after he completed the theory of general relativity (GR) [35]. In this framework gravitational waves arise from the time-varying quadrupole moment of a massive accelerating object. This is because the mass dipole moment is  $\vec{M} = \sum m_i \vec{r}_i$  and the gravitational field due to the dipole is given by its second time derivative. However, for a closed system the time derivative of  $\vec{M}$  is just the total momentum of the system, which is constant. So, the second time derivative of  $\vec{M}$  is zero, as is the gravitational field due to the dipole. Consequently, the quadrupole moment becomes the leading term in the multipole expansion [36]. Therefore, an important requirement for the production of GWs is that the source breaks spherical symmetry, ruling out single rotating stars as a viable source. Close binary systems of compact objects on the other hand, are excellent candidates for GW progenitors and can lose large amounts of energy and angular momentum by emitting GWs. So far, this object has to be a neutron star (NS) or a black hole (BH) in order to produce GWs of a magnitude sufficiently large to be detectable. When all surrounding matter has been ejected from such a binary system, the star remnants will spiral towards each other solely by emitting GWs. This process is exactly what leads to the binary neutron star (BNS) or NS-BH mergers and the possible SGRB that comes with it. It should be noted that detectable GWs can possibly be generated by core-collapse supernovae as well, provided that there is sufficient spherical asymmetry [37, 38]. This would enable researchers to study close supernovae and possible LGRBs with GW astronomy as well. Especially a galactic event would be an enormously valuable source of information in the view of multi-messenger astronomy. Core-collapse supernovae are expected to emit 99% of their energy as neutrinos ( $\sim 10^{53}$  erg), mostly in the MeV energy range [39, 40]. It has been demonstrated by the supernova event SN1987A in the Large Magellanic Cloud that such a neutrino excess by a nearby supernova can be observed [41].

### 2.2 Gravitational wave detection

The effect of GWs passing through a region of space can be described as periodically stretching space in one direction while compressing it in the perpendicular direction, in the plane orthogonal to the propagation direction. There are two different polarization directions along which the wave extends space, the one rotated over  $45^\circ$  with respect to the other [42]. These are called the “plus” (+) and “cross” ( $\times$ ) polarizations. In general, a wave is a combination of both<sup>3</sup>. So far the only way of directly detecting these perturbations is by laser interferometry. The basic principle is that a light beam is split by a beamsplitter into two “arms” of several kilometers long. Each arm contains a Fabry-Pérot cavity, which temporarily captures the light beam between two mirrors, called the Input Test Mass (ITM) and the End Test Mass (ETM). The Fabry-Pérot cavity is a multi-purpose component that amplifies the sensitivity for smaller phase shifts and reduces the effects of quantum fluctuations of the incident photon rate (known as shot noise). The beam travels back and forth through the arms several hundred times, before it escapes the cavity and recombines with the second beam at the beamsplitter. If both mirrors are placed an integer amount of wavelengths away from the beam splitter, both light beams will be in phase when they recombine and constructively interfere. The signal that leaves the beam splitter at the other side is detected by a photodetector. For convenience, the path length of one arm is shifted by half a wavelength, such that the beams destructively interfere and no signal is detected when the interferometer is in its ground state. When a gravitational wave passes through the interferometer, it will effectively make one arm shorter and the other one longer by a fraction of the size of a

---

<sup>3</sup>These are the so-called tensorial modes predicted by GR. Other theories can also involve two additional vector modes ( $x, y$ ) and two scalar modes ( $\circ, \ell$ ) [43].

proton. This will cause the light waves to not perfectly cancel out at the photodetector and a signal will be measured [44]. Such an interferometer is able to measure the amplitude and frequency of the wave, but not the directionality. This can be achieved by having several interferometers at different locations and measure the time difference between detection at the different sites. Knowing that gravitational waves travel at the speed of light [45], the position of the source can be reconstructed by triangulation. Currently, five interferometers are operational: The Laser Interferometer Gravitational wave Observatory (LIGO) in the US (one at Hanford and one at Livingston [46]), the Italian observatory Virgo [47, 48], the GEO600 observatory in Germany [49] and the Kamioka Gravitational observatory (KAGRA) in Japan [50], which began its first science run in February 2020.

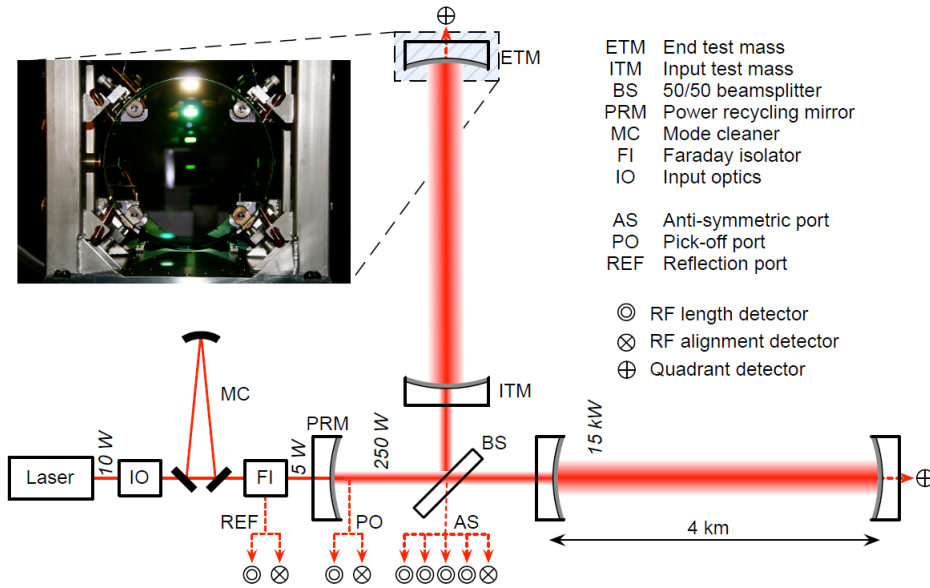


Figure 7: Schematic configuration of LIGO. From Abbott (2009) [46].

The first direct observation of a BNS merger was made by the LIGO/VIRGO collaboration in 2017 [51]. The GW event GW 170817 was quickly followed by GRB 170817A, detected by the Fermi satellite 1.74 seconds after the merger observed with GWs. The source was a binary merger with a total mass of around  $2.82^{+0.47}_{-0.09} M_{\odot}$ , within the mass range for neutron stars [52]. A sky localization analysis revealed a correlation between the position of both events, confirming that BNS mergers are the progenitors of at least some SGRBs. The early detection of the binary merger by LIGO/VIRGO allowed other telescopes to immediately follow up the merger on all wavelengths. In less than 11 hours an optical counterpart at 40 Mpc was discovered by the One-Meter, Two-Hemisphere (1M2H) team with the Swope telescope, and confirmed by many others [53, 54]. After 15 hours an ultraviolet transient was detected, which rapidly faded away over a two day period. After that the transient brightened in the infrared until a week after the merger. An X-ray source was found by the Chandra X-ray Observatory 9 days post merger [55] and finally, the transient was observed using radio wavelengths after 16 days [56]. The signature of the transient matched the expectations of a kilonova or macronova, similar to a supernova but dimmer and rapidly decreasing in luminosity. The optical and near-infrared transient of a kilonova is powered by the decay of heavy nuclei synthesised by rapid neutron capture (r-process), typical for the neutron rich environment [57]. The detailed analysis of the merger and its aftermath confirmed the existence of a kilonova and the associated large-scale production of heavy elements like gold, platinum and lanthanides [58–60]. The GRB however did not result in the detection of a neutrino in any of the neutrino observatories, resulting in an upper limit on the neutrino flux [61].

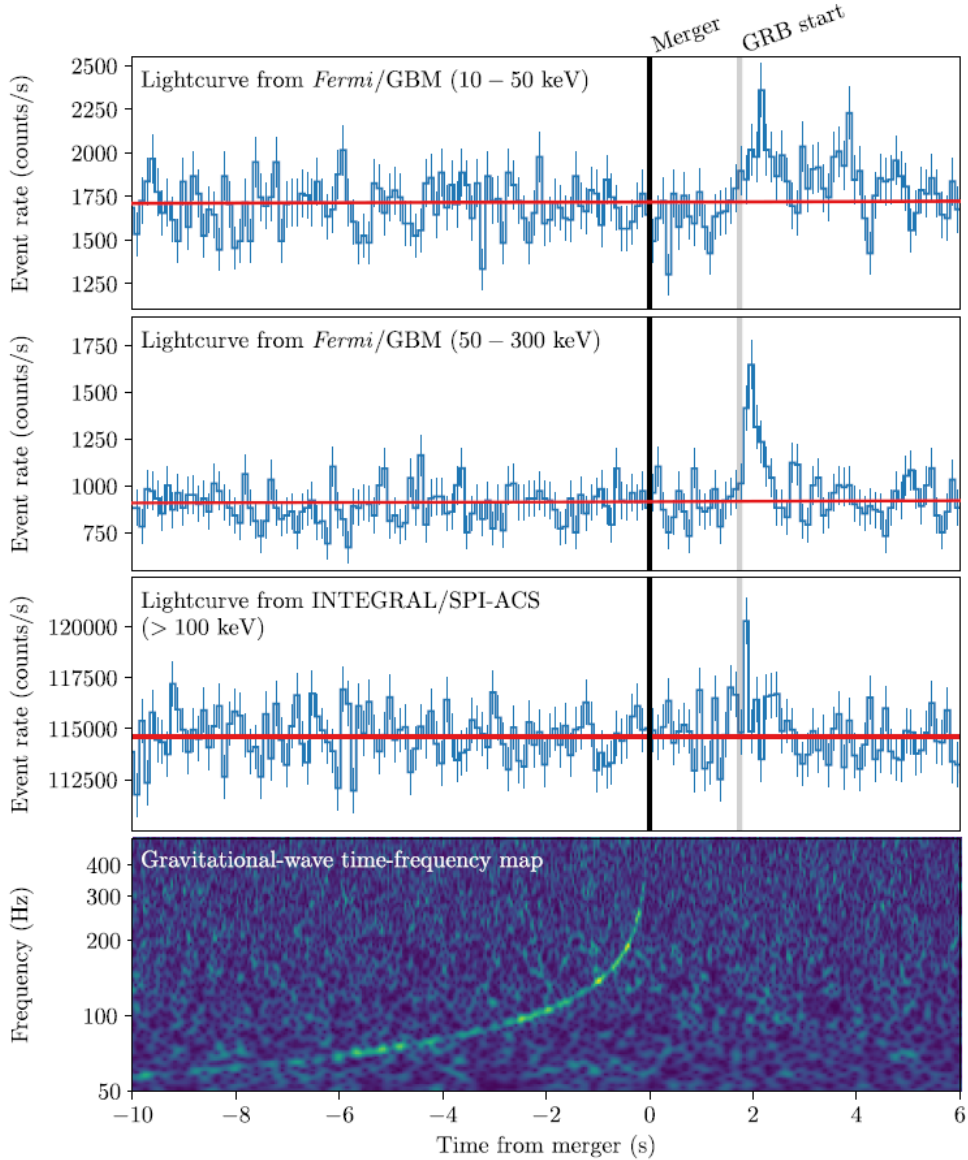


Figure 8: The light curves of GRB 170817A for different energy ranges and detectors and the frequency map of the corresponding gravitational wave signal GW 170817. The frequency of the GW signal quickly rises, leading up to the merger. The GRB starts 1.7 s later. From Abbott (2017) [45].

The introduction of gravitational wave astronomy has the advantage that the position of a GRB can be predicted beforehand up to some accuracy and that the progenitor masses can be estimated. In addition, the exact time of the merger can be determined and compared to that of neutrino or EM emission. GWs also give an additional constraint on the luminosity distance of GRBs. The amplitude  $h$  (or strain) of a gravitational wave in the Newtonian approximation is constrained by the chirp mass  $\mathcal{M} = \frac{(m_1 m_2)^{3/5}}{(m_1 + m_2)^{1/5}}$  and the source distance  $D$  [62]

$$h = \left(\frac{576}{5}\right)^{1/4} \pi^{2/3} Q(\theta, \phi, \psi, \iota) \frac{\mathcal{M}^{5/4}}{D} (t_c - t)^{-1/4} \cos\left(\int 2\pi f dt\right). \quad (18)$$

The function  $Q$  depends on the angular position of the source  $(\theta, \phi)$  and the orientation of the binary  $(\psi, \iota)$ . The frequency  $f$  of the signal increases with time  $t$  until the merger happens at  $t = t_c$ . The chirp mass can be determined from the frequency wave spectrum alone

$$\dot{f} = \frac{96}{5} \pi^{8/3} \mathcal{M}^{5/3} f^{11/3}, \quad (19)$$

such that the distance can be found by analysing the time evolution of the strain [63]. Note that the  $Q$  function requires the position and the orientation of the source, for which ideally a network of three or more detectors is needed.

## 2.3 Third-generation interferometers

### 2.3.1 Einstein Telescope

The L-shaped geometry of current detectors has the drawback that they have blind spots when the wave passes through the plane of the interferometer at a  $45^\circ$  angle with respect to the arms. This issue is partly resolved by nesting three detectors in a triangular shape at one location, as will be the case for the Einstein Telescope (ET). The observatory is expected to be operational in the mid 2030s and will be located either in Sardinia, Italy or in the three-border region of Belgium, Germany and the Netherlands [64].

The sensitivity of an interferometer is quantified by the antenna pattern functions  $F_\times$  and  $F_+$ , one for each polarization. The response function  $h$  for a GW with wave amplitudes  $h_\times$  and  $h_+$  can be written as

$$h(t) = F_+(\theta, \phi, \psi) h_+(t) + F_\times(\theta, \phi, \psi) h_\times(t). \quad (20)$$

The angles  $(\theta, \phi)$  describe the angular position of the source in the sky and  $\psi$  is the polarization angle of the wave. The quantity  $F = \sqrt{F_\times^2 + F_+^2}$ , called the antenna pattern, is averaged over  $\psi$  and therefore quantifies the relative sensitivity of the detector for a certain position in the sky [65, 66]. The value of  $F$  cannot exceed 1 for a single detector, but it can for three nested detectors, as shown in Figure 9. It can also be seen that ET will not have the four blind spots that Virgo or LIGO have, but rather have a band with slightly decreased sensitivity along the detector plane. Along this band, the antenna pattern of ET is still around 60% of the maximal value in an L-shaped interferometer. Note that the antenna pattern of a detector only quantifies the directional sensitivity relative to the maximal sensitivity of said detector. So even though the pattern function is only around 0.6 in some areas, ET will still be able to detect smaller wave amplitudes in these areas than Virgo or LIGO can anywhere. In addition, the antenna pattern does show the obvious advantage of three nested detectors compared to a single L-shaped detector of the same size.

Each of the ET detectors consists of two interferometers, one for high frequencies and one for low frequencies, as shown in Figure 10. The high-frequency component is mostly the same as current interferometers, with the lower end of their frequency spectrum dominated by thermal noise. This thermal noise is avoided in the low-frequency component by cryogenic cooling, but this, in turn, introduces a higher amount of quantum noise (or shot noise) in the high-frequency range. Both components thus complement each other to broaden the frequency range. Each interferometer will have arms of 10 km, magnifying the effect of mirror displacement by GWs. The observatory will be placed 100 m underground to mitigate any Newtonian noise effects, which are amplified at the surface [67]. In the end, ET is expected to be 10 times more sensitive than the LIGO/Virgo facility in the medium to high frequency range ( $> 30$  Hz) and 100 or more times more sensitive in the low frequency range.

This improved sensitivity has two main advantages. First of all, it will extend the range at which compact mergers can be seen. Second, the signal will be noticed much earlier, when the wave amplitudes are weaker and the frequencies lower.

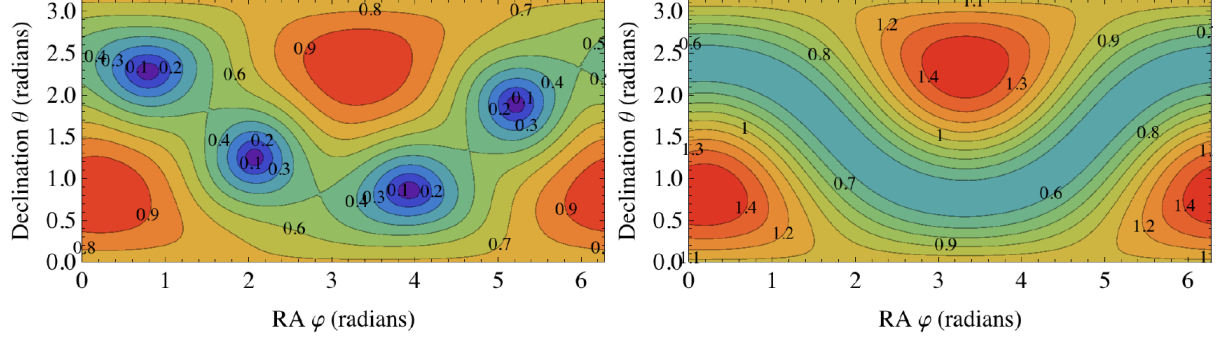


Figure 9: The antenna pattern for Virgo (left) and ET (right) assuming conventional GWs with tensorial polarizations. With the three nested interferometers, ET can reach up to 1.5 times the maximal sensitivity that a single 10 km L-shaped interferometer can reach at its hotspot. At the same time the sensitivity will not drop below 50% of that same maximum. From Abernathy (2011) [68].

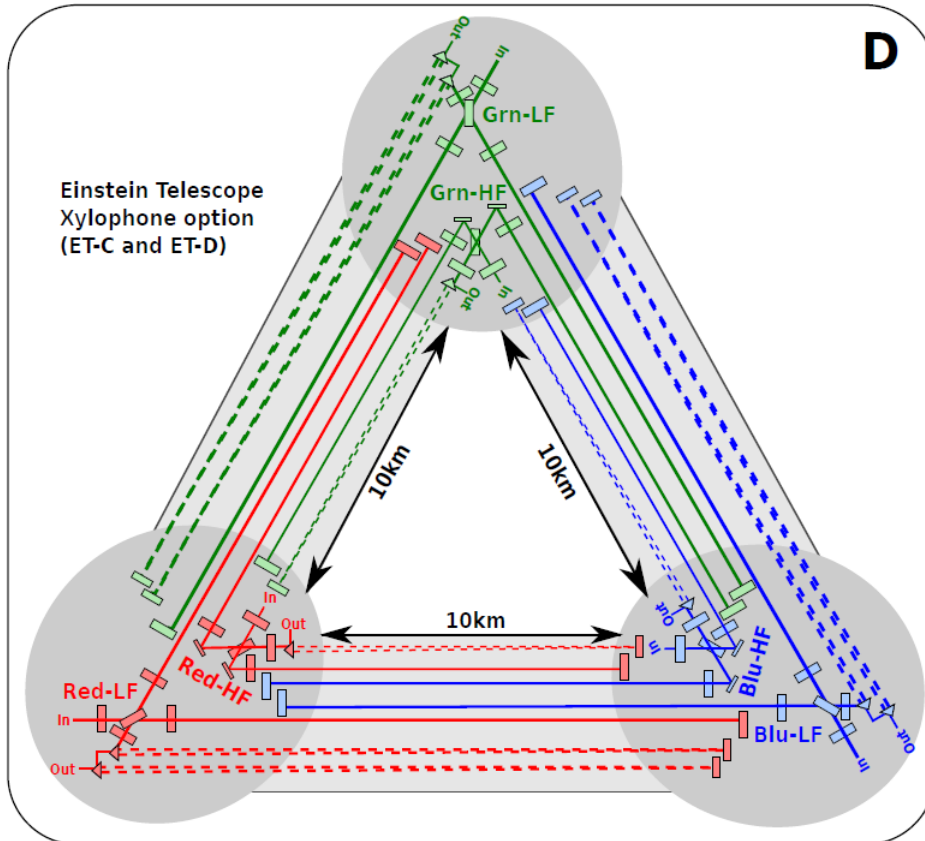


Figure 10: The triangular configuration of the Einstein telescope. The three nested detectors, each consisting out of a high-frequency (HF) and low-frequency (LF) interferometer, share three 10 km arms. From Hild (2011) [69].

In the context of GRBs, it is interesting to analyse BNS mergers. Because of GW 170817 it is known that BNS mergers can produce GRBs, and perhaps NS-BH mergers can as well. The coalescence rate of compact binary mergers observable by ET is expected to increase greatly compared to current detectors, especially for BNS mergers. With a sensitivity that is 10 times greater, a BNS merger can be detected 10 times further away, since the amplitude of GWs decreases as the inverse of the distance (and not the distance squared as for electromagnetic radiation). This means that a volume that is 1000 times larger can be searched. Besides the larger volume in which ET can detect mergers, star formation is enhanced between  $z \sim 1 - 3$  [70]. This can lead to BNS merger rates of around  $7 \times 10^4 \text{ yr}^{-1}$  for redshifts up to  $z \sim 2$  [64, 71]. As a reference, Advanced LIGO at its design sensitivity will have a BNS detection range of  $\sim 220 \text{ Mpc}$  ( $z \simeq 0.05$ ). Although additional upgrades are proposed that could double that range for LIGO [72]. Depending on the opening angle of SGRBs and the available network of telescopes, about  $10^2 - 10^3$  BNS mergers can be detected with an optical counterpart over a few years of operation time with ET [71].

### 2.3.2 Cosmic Explorer

Another proposed third-generation interferometer worth mentioning, is the Cosmic Explorer (CE) in the US. Unlike ET, the Cosmic Explorer will be a traditional L-shaped interferometer with 40 km arms, relying on the well-proven efficiency of the current LIGO/Virgo detectors [73]. It will (initially) not profit from an extended frequency range like ET and suffer from the blind spots along the detector plane. However, in the high-frequency range, CE will be more sensitive than ET. The first stage of CE will ideally be ready to start observation in the 2030s and undergo several upgrades concerning the core optics, entering the second stage in the 2040s. In co-operation with ET and current detectors, the Cosmic Explorer will be part of a powerful network of interferometers, which can be used to accurately identify and triangulate GW sources.

### 3 Neutrino detection with IceCube

#### 3.1 The IceCube detector

The IceCube neutrino observatory consists of a cubic kilometer of clear ice at the South Pole [74, 75], equipped with 5160 Digital Optical Modules (DOMs) that can detect Cherenkov light using a Photo-Multiplier Tube (PMT). The DOMs are attached to vertical strings which are placed on a hexagonal grid with 125 m of horizontal spacing. Each of the 86 strings holds 60 DOMs with a nominal vertical separation of 17 m. This network of Cherenkov detectors covers the IceCube detector volume at a depth between 1450 m to 2450 m. With this setup it is possible to detect neutrinos with an energy larger than 100 GeV [76]. In the central region of IceCube, called DeepCore, the DOMs are more closely packed together with only 7 m of vertical spacing and a horizontal spacing between strings of 42 m to 72 m. This allows the DOMs to detect signatures of neutrinos with an energy as low as 10 GeV [77]. On the surface above IceCube, an array of Cherenkov detectors is present with the objective of detecting cosmic-ray induced air showers. This array, called IceTop, consists of 162 cylindrical tanks of 1.3 m high filled with an ice mass of 1.8 m diameter and 90 cm high. The Cherenkov radiation of charged particles passing through a tank is monitored by two DOMs, similar to the main IceCube detector [78, 79]. The amount of tanks exhibiting a signal is proportional to the energy of the parent cosmic-ray particle, whereas the time difference between the tank signals allows for a directional reconstruction. An artist impression of the IceCube observatory is shown in Figure 11.

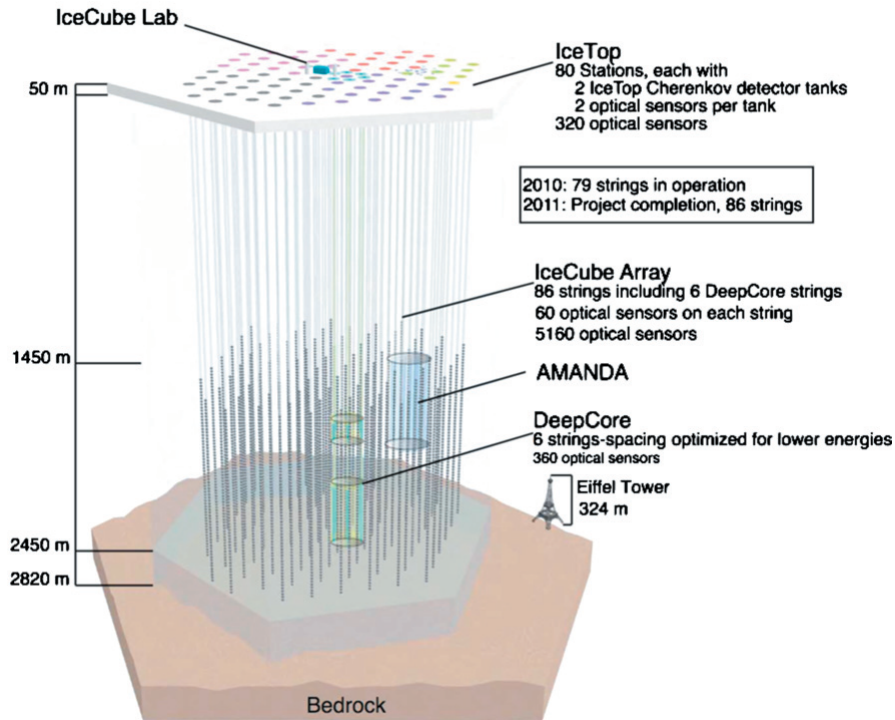


Figure 11: The design of the IceCube detector along with DeepCore. Its predecessor AMANDA, consisting of 667 optical modules on 19 strings, is shown as reference [80]. From Halzen (2010) [76].

### 3.2 Neutrino cross sections

Neutrinos interact with atomic nuclei in the ice either by Charged or Neutral Current (CC or NC) interactions. The NC interaction is mediated by a Z-boson and results in a hadronic cascade while the CC interaction also produces a same-flavoured charged lepton.

The need for a detector of this size is justified by the extremely small interaction rate of neutrinos, as indicated in Figure 12. The estimated number flux of neutrinos is around  $6 \times 10^{10} \text{ cm}^{-2} \text{ s}^{-1}$  and almost entirely dominated by solar neutrinos [81]. Typical energies for solar neutrinos are a few hundreds of keV up to 20 MeV, below the energy range for which IceCube is sensitive [82]. Other populations of neutrinos include atmospheric neutrinos originating from the decay of pions and kaons induced by Cosmic-Ray (CR) interactions. The largest part of neutrino events detected by IceCube in the 10 GeV to 100 TeV energy range are the result of atmospheric neutrinos. Beyond that the spectrum shows a deviation from the power law caused by astrophysical neutrinos, as outlined below.

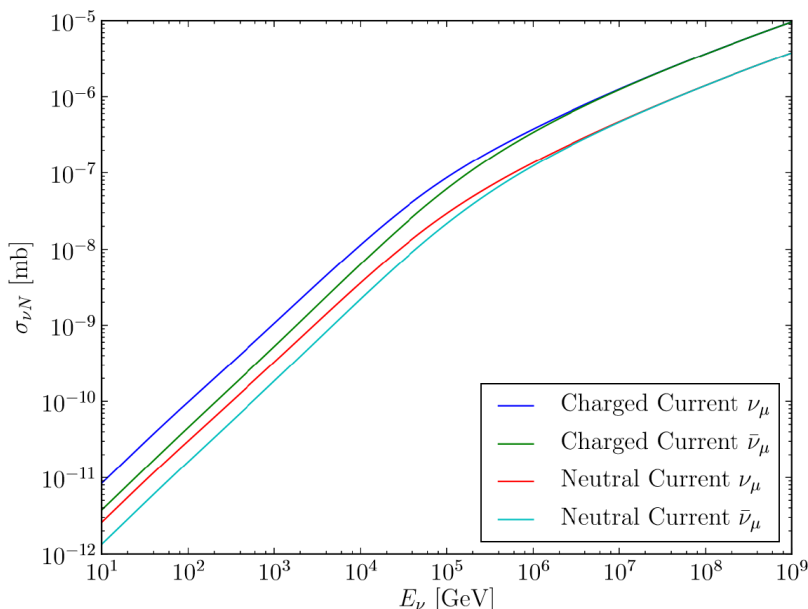


Figure 12: Energy-dependent cross sections of (anti-)neutrinos for both charged and neutral current interactions with nuclei. From [83].

### 3.3 Event selection

The challenge is to distinguish background neutrinos from the astrophysical neutrinos from a GRB. In the energy range for which IceCube is sensitive, the background spectrum is dominated by atmospheric neutrinos up to about 100 TeV. An efficient method to eliminate this background is to impose a lower energy threshold and only consider the neutrino events with a reconstructed energy above this threshold. The selected neutrinos are then most likely of astrophysical origin. In the view of astrophysical point sources like GRBs, it is necessary to accurately reconstruct the arrival direction of the neutrino. Only muon neutrinos are fit for this purpose, since the secondary muon travels far enough to leave a detectable track in the detector. The secondary electron from  $\nu_e$ -interactions cannot travel far because of scatterings and induces an electromagnetic cascade with little to no directionality. The tauons from the  $\nu_\tau$  interactions quickly decay such that the track terminates and triggers a second cascade. Secondary muons on the other hand can traverse the entire detector before decaying.

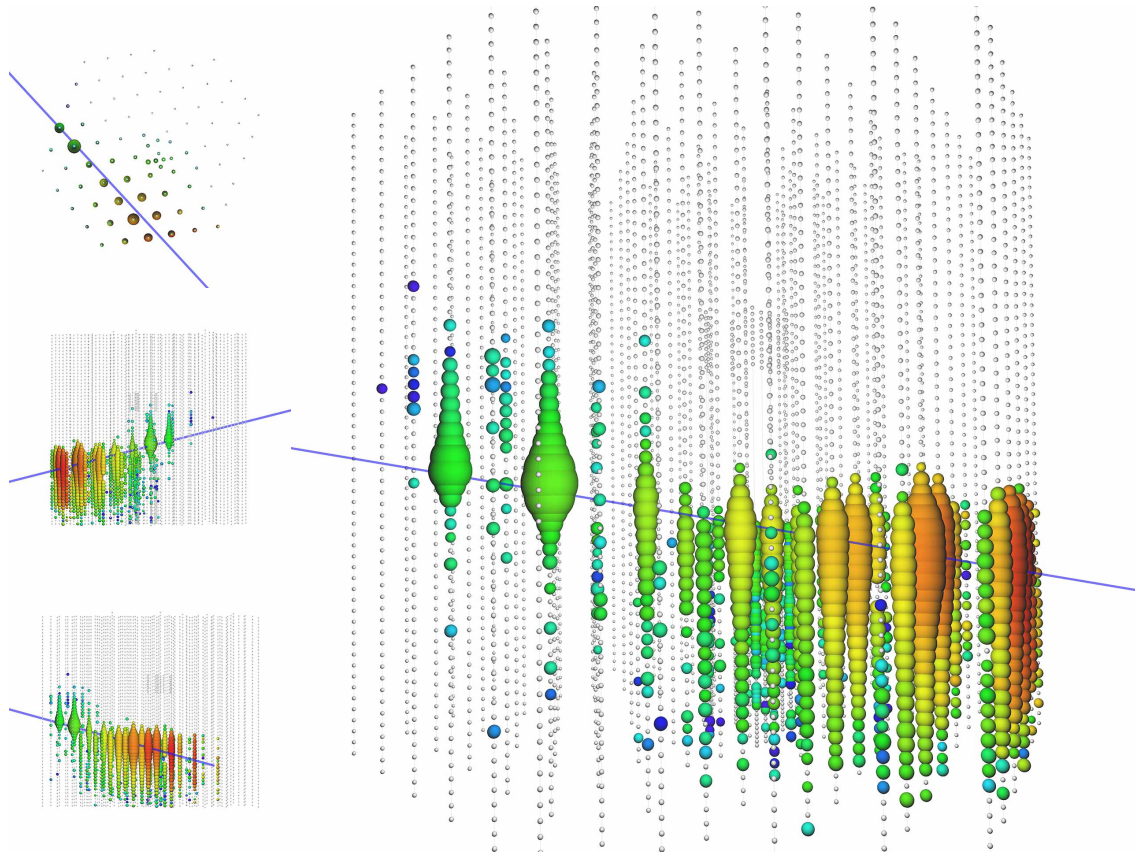


Figure 13: A track-like event in IceCube. Red spheres indicate an earlier photon arrival time and later arrival times shift more towards green. The size of the spheres scales logarithmically with the charge measured by the PMT. The blue line is the reconstructed path of the muon. From Aartsen (2016) [84].

In addition, the scattering angle between the neutrino and the muon decreases for higher neutrino energies and is typically below  $1^\circ$  for the energies that exceed 10 TeV. The downside is that there is a lot of muon background in the detector coming from cosmic-ray interactions in the atmosphere. Conveniently, the Earth can be used to shield the detector from atmospheric muons, since muons cannot traverse the large distances through matter like neutrinos can. This is why only up-going muons are included in the analysis, as they have to be induced by a neutrino interaction. For the specific case of GRBs (or any astrophysical point source) the background can be further reduced by only accepting events with an angular position close to the GRB position. By restricting oneself to a patch of a few degrees around the GRB, the background can be greatly reduced while keeping most of the signal neutrinos. This is again why the muon tracks are needed to determine the source location. Because of the burst-like nature of the event, it is natural to only include the events within a small time window around the burst trigger time. With the largely reduced background the energy threshold can then be relaxed to get more statistics.

### 3.4 The astrophysical neutrino spectrum

A quantity closely related to fluence is the flux  $F$ , defined as the number of particles ( $N$ ) per unit surface ( $A$ ) per unit time

$$F = \frac{dN}{dAdt}. \quad (21)$$

The source intensity  $\Phi = \frac{dF}{d\Omega}$ , the flux per solid angle, is another useful quantity from a theoretical perspective. This is because the flux received from a source within a solid angle  $\Omega$  is a distance-independent quantity. The flux itself decreases as the inverse square of the distance to the detector ( $\sim r^{-2}$ ), as does the subtended solid angle of a source with fixed dimensions. Dividing (or differentiating) the flux by the solid angle effectively eliminates the dependence on the distance. However, the source intensity is not a relevant quantity for measuring individual GRBs, which are supposed point sources with an infinitesimally small solid angle. A diffuse flux on the other hand, can be well-described by the source intensity.

The so-called differential flux  $\frac{d\Phi}{dE}$  is the flux density within a certain energy range  $dE$  per unit of solid angle. The differential flux, as a function of neutrino energy, shows a power law behaviour, which is why it is often scaled with  $E^\alpha$

$$\frac{d\Phi}{dE} = \Phi_0 \left( \frac{E}{E_0} \right)^\alpha. \quad (22)$$

A typical choice for the spectral index is  $\alpha = -2$ , since Fermi shock acceleration predicts such a spectrum. However, as mentioned before, more detailed simulations of ultra-relativistic shocks report a steeper spectrum with  $\alpha \simeq -2.2$  to  $-2.3$  [29]. The differential flux is then defined by the flux normalisation  $\Phi_0$  alone, often scaled by a well-chosen energy scale  $E_0$ . It is then straightforward to convert the flux, measured during a certain time interval  $\Delta t$  over a solid angle  $\Omega$ , to fluence units

$$S_0 = \Omega \cdot \Delta t \cdot \Phi_0. \quad (23)$$

One of the latest analyses of IceCube data from 2009 through 2018 involved over 650 000 reconstructed neutrino events with energies ranging from a few TeV up to 10 PeV. The data is fitted by an unbroken power law with spectral index  $\alpha = -2.28_{-0.09}^{+0.08}$  and a flux normalisation at 100 TeV neutrino energy of  $\Phi_0 = 1.44_{-0.24}^{+0.25} \times 10^{-8}$  (GeV cm<sup>2</sup> s sr)<sup>-1</sup> [85]. Some of the past data samples used for the reconstruction of the neutrino spectrum are shown in Figure 14. The events included in the analysis are limited to up-going muon events to profit from the atmospheric muon shielding provided by the Earth.

Earlier analyses where only neutrinos with a reconstructed energy above 200 TeV are considered, report a harder spectrum with spectral index  $\alpha = -2.13 \pm 0.13$ . This might indicate a break in the spectrum due to a change in the production mechanism of neutrinos at a certain energy. Some GRB models predict such an energy break for neutrinos, however, the observed tension is currently not (yet) strong enough to uncover a definitive shift in the spectral index [86].

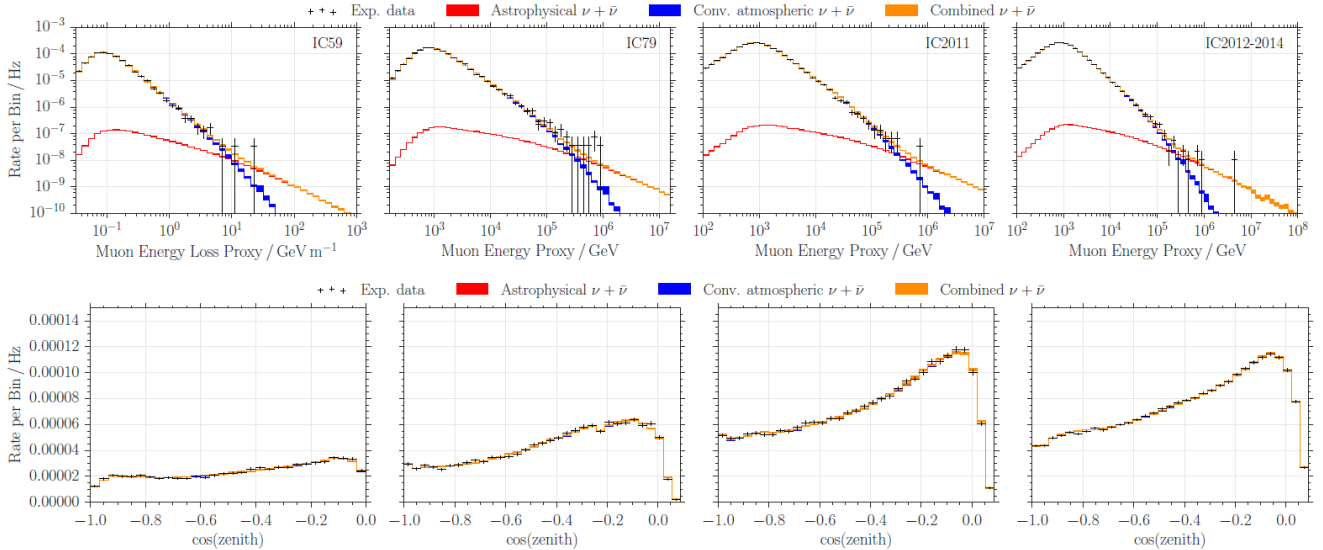


Figure 14: Event rates for different IceCube data samples labeled by the amount of DOM strings operational at the time of observation (i.e. 59 strings for IC59, 79 strings for IC79 and the full 86 string configuration for IC2011 and IC2012-2014). The best-fit astrophysical and atmospheric neutrino spectra are shown as full lines. The distribution of the data samples as a function of zenith angle is shown below. From Aartsen (2016) [84].

### 3.5 Simulating neutrino interactions

It is not straightforward to predict the amount of detectable events from a certain flux passing through the detector volume. Many effects like imperfections in the ice, PMT detection efficiencies, shielding by the earth, etc. combined with the energy-dependent neutrino-nucleon cross-section give a distorted image of the actual astrophysical flux. For this reason, simulations are carried out with a pre-defined neutrino flux that take all of these effects in account. Neutrinos are sampled from a power-law spectrum and generated on the earth's surface, in the direction of IceCube. Of course nearly all of them would propagate through the earth unseen, and an infeasible amount of neutrinos would have to be generated to get any of them to interact. Instead, all generated neutrinos are forced to interact, regardless of their energy and whether or not their interaction would result in detectable signal.

In order to get reasonable information out of the IceCube simulations, the output data is given in terms of the physical parameters of the primary neutrino (energy, declination, right ascension,...) as well as for each event a OneWeight ( $OW$ ). These weights have the property that, when they are multiplied by a differential flux, their sum gives the event rate at which particles are expected to be observed in the detector

$$\dot{N} = \sum_i OW_i \times \left. \frac{d\Phi}{dE} \right|_{E=E_i}, \quad (24)$$

where the sum runs over all simulated events. This means that each individual weight is multiplied by the flux for which the expected observations are simulated (usually of the form  $\Phi_0 E^{-2}$ ) evaluated at the energy of the simulated neutrino. Note that all information of the simulation like detector geometry and interaction cross-sections are contained within these weights. So a neutrino that would be relatively likely to interact will have a larger  $OW$  than one with a low interaction probability. This means that the weights are energy-dependent, since a higher-energy neutrino has a larger cross section.

As mentioned before, the differential flux is not a convenient quantity when it comes to point sources like GRBs. Equation (24) can be slightly modified if the fluence of a burst is to be investigated, by only considering the simulated events close to the GRB position in the sky. In this scenario the angular dependence of the detector acceptance can start to play a role. This is investigated by dividing the celestial sphere into narrow declination bands. Since the IceCube detector has azimuthal symmetry there should be no difference for GRBs that belong to the same declination band. Consequently the sum in Equation (29) is limited to all events within this declination region. To account for the different size of each band the weights are normalised by the solid angle subtended by the corresponding declination band. After multiplying the fluence with the weights of all simulated events within this band, their sum gives the total number of detected neutrinos from the GRB

$$N = \sum_i \frac{OW_i}{\Omega_{\Delta\theta}} \times \left. \frac{dS}{dE} \right|_{E=E_i}. \quad (25)$$

For a given band starting at declination  $\delta$  and ending at declination  $\delta + \Delta\theta$  the solid angle is given by

$$\Omega_{\Delta\theta} = 2\pi(\sin(\delta + \Delta\theta) - \sin \delta). \quad (26)$$

If each band has the same width  $\Delta\theta$ , then naturally the bands close to the horizon will have the largest solid angle because of the larger circumference. Another way to look at it is by means of the effective area  $A_{\text{eff}}$  defined as the fraction between the observed event rate  $\dot{N}$  and the incoming flux  $F$

$$A_{\text{eff}} = \frac{\dot{N}}{F}. \quad (27)$$

For a perfect detector, meaning 100% efficient at detecting neutrinos in all directions, this would simply be the cross-sectional area of the detector. In reality, all effects mentioned above have to be accounted for and the observed event rate is less than what you would expect from the flux. The effective area is the bridge to go from the event rate that is measured, to the flux that one would like to know. Just like the weights, the effective area is energy-dependent, as shown in Figure 15 where one observes the effect that the Earth becomes opaque for neutrinos at energies above 100 TeV.

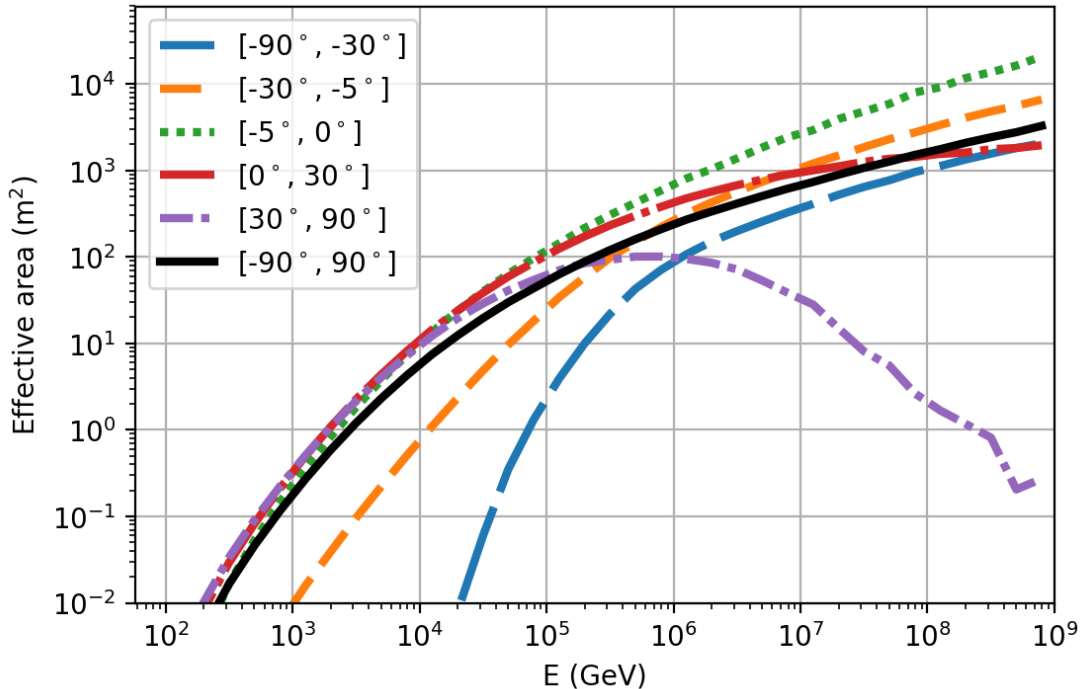


Figure 15: The effective area of IceCube for different declination bands.

### 3.6 Detector sensitivity

Simulated data can be used to quantify the performance of an IceCube GRB analysis. Assuming that the distribution of background events is known, the number of signal events required to observe a significant statistical excess can be determined by adding simulated signal events to the background sample. Using this approach, the sensitivity and discovery potential of the analysis can be determined, as outlined below.

Assume a test statistic  $T$ , which is a function of a set of physical observables  $X$  and takes a value  $T = T_X$ . Naturally, this test statistic is subject to statistical fluctuations in  $X$ , since repeating the experiment may result in a different set of observables  $X'$  and a different test statistic  $T = T_{X'}$ . The Probability Density Function (PDF) of the test statistic is  $\mathcal{T}(\lambda|\theta)$  for a value  $T = \lambda$  and a given set of physical parameters  $\theta$ . The parameters  $\theta$  are initially unknown and to be extracted from the experiment. Based on the resulting value  $T_X$  from the experiment (or simulation), it can be checked to what extent this value agrees with a given hypothesis  $\mathcal{H}$ . This hypothesis defines the shape and characteristics of the PDF, like the expectation value, variance, etc. and corresponds to a fixed set of physical parameters  $\theta$ . The p-value of a particular outcome  $T = T_X$  is defined as the probability that the test statistic will exceed this value when the experiment is repeated

$$p = P(T \geq T_X|\mathcal{H}) = \int_{T_X}^{\infty} \mathcal{T}(\lambda|\theta) d\lambda = 1 - \int_0^{T_X} \mathcal{T}(\lambda|\theta) d\lambda, \quad (28)$$

for a specified hypothesis  $\mathcal{H}$ . Consequently, a low p-value is an indication that the underlying hypothesis is false. In particular, if one assumes the background-only hypothesis  $\mathcal{H}_0$ , then  $p$  quantifies the plausibility to identify the data set  $X$  with a pure background. If  $p$  is small enough, then  $\mathcal{H}_0$  can be rejected and the data is likely to contain signal events in addition to background.

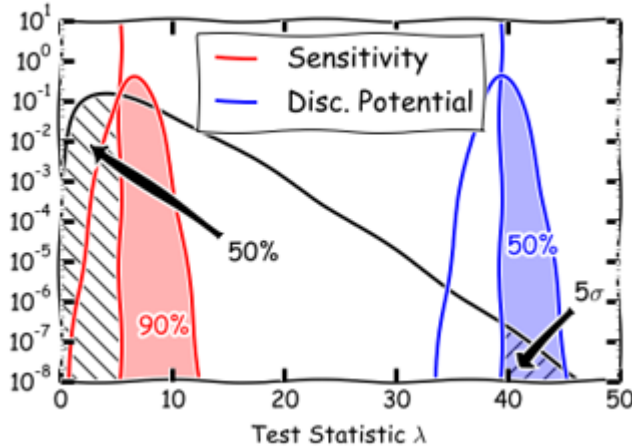


Figure 16: Schematic to illustrate the definitions of sensitivity and discovery potential. The background-only PDF is shown in black and the PDFs corresponding to the sensitivity and discovery potential are shown in red and blue respectively [87].

From here on, the p-value will refer to the definition in Equation (28) applied to the background-only hypothesis. The background-only PDF will be denoted as  $\mathcal{T}_0$  and the signal+background PDF as  $\mathcal{T}_s$  for a certain amount of injected signal  $s$ .

The sensitivity is the amount of signal events  $s$  required such that in 90% of the experiments, a value  $T = T_s$  is sampled from  $\mathcal{T}_s$ , which has a p-value of at most 50%. A sample with a p-value of 50% is simply the median of the background-only distribution  $\mathcal{T}_0$ . So the sensitivity corresponds to the amount of signal that will result in a value  $T_s$  that is above the background median in 90% of the test samples. The discovery potential (DP) is defined as the expectation value of the test statistic for which 50% of the values drawn from the PDF will have a p-value of at most  $5 \times 10^{-7}$ , corresponding to a  $5\sigma$  effect in case of a single-sided Gaussian distribution. The DP corresponds to the amount of signal required to claim a  $5\sigma$  discovery with a 50% probability<sup>4</sup>.

In the example of neutrino simulations, the total signal+background event count within a certain time interval is considered to be the test statistic. The signal event rate, given in Equation (24), depends on the OneWeights, which constitute the set of observables  $X$  in the analogy with test statistics. In the case of a power-law spectrum the only free parameter is the flux normalisation  $\Phi_0$ , assuming a spectral index of  $-2$ . So for a given set of simulated data (providing  $E_i$  and the weights  $OW_i$ ) the event rate is given entirely in function of the normalisation

$$\dot{N} = \Phi_0 \sum_i OW_i \times E_i^{-2}. \quad (29)$$

Since the appearance of neutrinos is a Poisson process, the probability to obtain  $k$  neutrinos in a time interval  $\Delta t$  is given by

$$P(k \text{ events}) = \frac{(r\Delta t)^k}{k!} e^{-r\Delta t}, \quad (30)$$

where the average neutrino rate is given by  $r$ . It is assumed that the background rate  $r_{\text{bkg}}$  is small enough such that the probability of detecting zero background events is larger than 50%, during the time interval  $\Delta t$ .

<sup>4</sup>To be exact, this is the 50% DP at  $5\sigma$  significance. But it is often taken to be the standard in (astro)particle physics.

The background-only hypothesis thus implies a Poisson distribution with a median of 0. We want to know how much signal has to be injected such that at least 90% of the samples result in a number of events larger than the background median, i.e. at least one event. The probability to obtain at least one neutrino in the time interval  $\Delta t$  can be written as:

$$\begin{aligned} P(k \geq 1) &= 1 - P(k = 0) \\ &= 1 - e^{-r\Delta t}. \end{aligned} \tag{31}$$

A probability of 90% is required for the event rate that corresponds to the sensitivity. Then  $r\Delta t$  is constrained by  $1 - e^{-r\Delta t} = 0.9$ , or equivalently  $r\Delta t \approx 2.3$ . This means that for an experiment where on average 2.3 neutrinos are obtained, there is a 90% chance to detect at least one event. Or a series of these experiments will result in the detection of at least one event 90% of the time. Thus, the sensitivity for the event rate becomes  $r = 2.3/\Delta t$ . This illustrates that a longer observation time lowers the sensitivity, and the detector becomes sensitive to much lower event rates. On the other hand, the number of background events is expected to increase linearly with the observation time. So there is a point where  $\Delta t$  becomes too large and the median of the background distribution becomes larger than zero.

Since  $\Phi_0$  defines the event rate (see Equation (29)), the sensitivity can equally well be given by this parameter. Consider a detection time of 1000 s during which a neutrino flux is measured, as will be the standard for GRB analyses in relation with GW events, such that the sensitivity is  $\dot{N} = \frac{2.3}{1000}$  Hz. The normalisation of the required flux, according to Equation (29), is  $\Phi_0 = 5.10 \times 10^{-6} \text{ GeV}^{-1} \text{ cm}^{-2} \text{ s}^{-1} \text{ sr}^{-1}$ . This can be interpreted as the minimal full-sky flux that can be distinguished from background with a 90% significance. Thus, the detector is said to have a flux sensitivity corresponding to  $\Phi_0$ .

However, when studying GRBs we want to consider point sources with a well-defined position in the sky, instead of a diffuse flux. If the sky is divided into declination bands of equal width, than Equation (25) and (26) can be used to calculate the sensitivity in terms of the fluence as a function of declination. The width of the bands  $\Delta\theta$  is taken to be  $1^\circ$ . For the differential fluence, one can also assume an  $E^{-2}$  spectrum such that

$$N = \frac{S_0}{\Omega_{\Delta\theta}} \sum_i OW_i \times E_i^{-2}. \tag{32}$$

The number of detected neutrinos at sensitivity level is still  $N = 2.3$ . The corresponding fluence normalisation is presented in Figure 17.

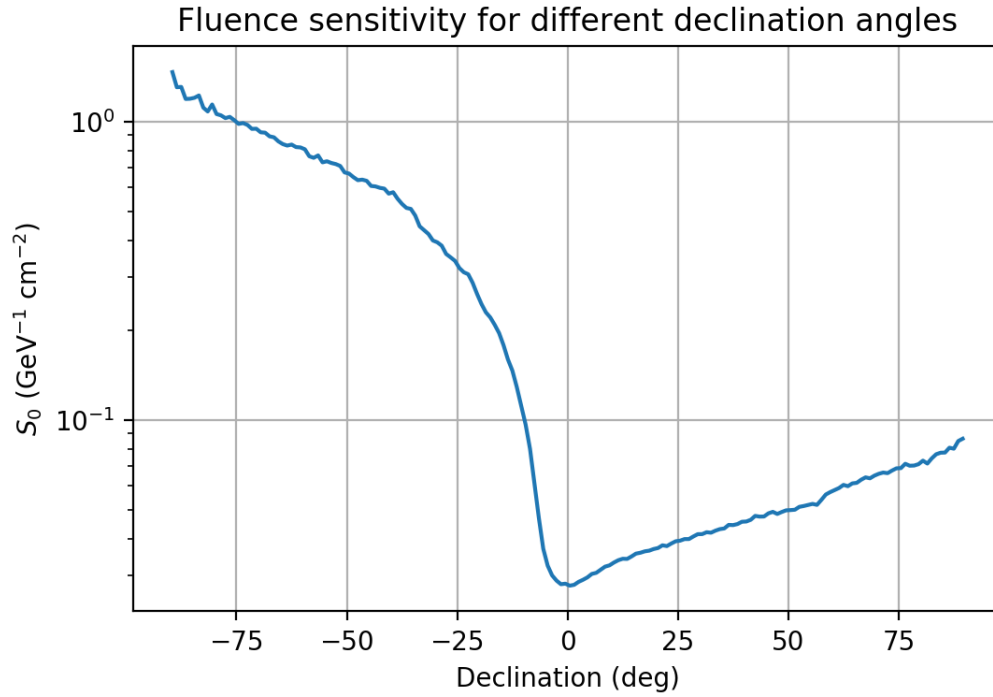


Figure 17: Fluence sensitivity for an  $E^{-2}$  spectrum with a normalisation  $S_0$  at  $E_0 = 1$  GeV. The x-axis is divided into bins of  $1^\circ$  declination and the result is normalised by the solid angle subtended by the band at this declination. Note that the sensitivity of the detector is much better at the Northern Hemisphere (i.e. positive declinations) since the Earth shields IceCube from atmospheric muons.

## 4 NcAstrolab toy model

To make predictions on the detectability of a neutrino excess from BNS mergers, the NcAstrolab class of the ROOT-based NCFSPack framework is utilised (for documentation, see [88]). The class represents a virtual lab with a customizable terrestrial position and timestamp. In this case IceCube is the lab of choice, located at the South Pole. A neutrino event is characterised by its position on the celestial sphere and a timestamp at which the neutrino is detected. For the toy model presented here, the neutrinos will originate from a collection of GRBs, of which the parameters can be entirely user-defined. Some relevant parameters are

- The number of bursts accepted for analysis
- The average, minimal and maximum  $T_{90}$  of the burst to be accepted for analysis
- The minimal and maximal declination of accepted bursts
- The angular uncertainty on both the burst position and the reconstructed neutrino trajectory
- The redshift distribution of the burst population
- The mean background rate of neutrino events
- The time window during which neutrino events are accepted for analysis
- The average fraction of GRBs that will trigger a neutrino detection in IceCube, or equivalently, the probability that a single GRB will result in the detection of a neutrino in IceCube
- The distribution of the neutrino arrival time  $\tau$  relative to the burst trigger, with an average  $\mu_\tau$  and a spread  $\sigma_\tau$ .  $\tau$  is assumed to follow a normal distribution

### 4.1 Time profile stacking

The toy model sets a time window  $[t_0 - \Delta t, t_0 + \Delta t]$  around the time  $t_0$  of each GRB trigger. Unless otherwise specified, a time window of 500 s before and after the GRB trigger will be employed. This is motivated by the fact that there are hardly any bursts with a duration that exceeds 500 s (disregarding afterglow). In the pre-burst window there have been findings of precursors events, but these typically occur less than 200 s before the burst trigger [89]. In order to symmetrise the time window, it is extended to -500 s. In this time interval, background neutrinos are sampled from a Poisson distribution with an average rate of 3 mHz for the entire Northern Hemisphere, according to the irreducible atmospheric neutrino background rate detected in IceCube. The relative arrival times of these background neutrinos are then uniformly distributed around  $t_0$ . The angular positions of the background events are uniformly distributed on the hemisphere as well.

With the time profile stacking procedure [90], all of these time windows and their content are stacked onto each other. If the sample size of GRBs is large enough, one can hope to find a statistically significant excess of neutrinos above the background levels, as shown in Figure 18. In this specific example 1000 GRBs are randomly generated with an average neutrino rate of 0.03 per burst. The signal neutrinos are generated 90 s after the burst trigger with a spread of 15 s. A clear excess of neutrinos around the GRB positions is seen compared to the background region.

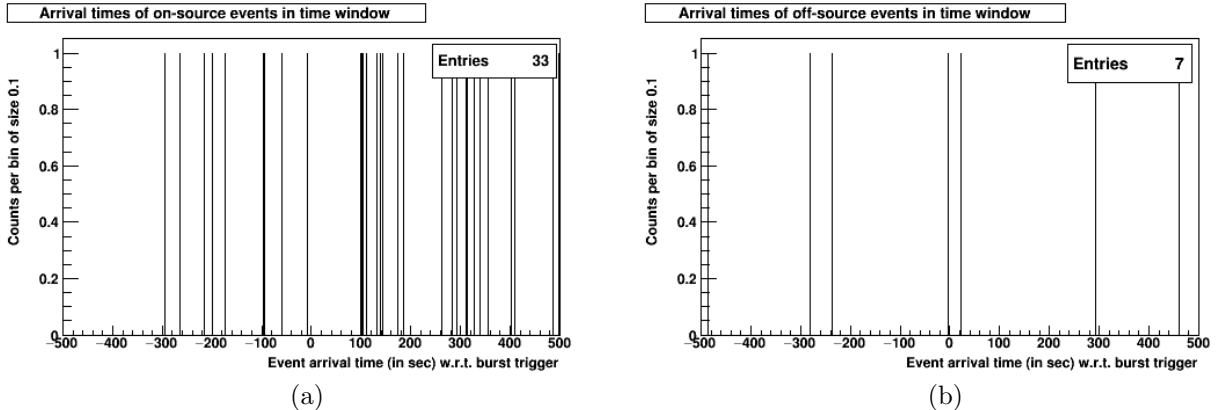


Figure 18: Left: The stacked arrival times of neutrinos within a patch of sky around each GRB position (“on-source”). This includes both background and signal neutrinos. Right: The stacked arrival times of neutrinos inside a patch of sky at the same declination as the individual sources, but at opposite right ascension (“off-source”). Due to the cylindrical symmetry of IceCube, this should be representative for the background on the source. Both the on-source and off-source regions accept neutrinos within  $5^\circ$  of the burst position.

If instead, the GRB position is determined by the means of gravitational waves by ET, one can still use the same methodology. The main difference is that ET is expected to detect significantly more BNS mergers than Fermi or similar experiments. In the case of a BNS merger, the center of the time interval will be taken at the time of the merger. Unlike a GRB, the moment in time when the neutron stars merge is very well defined. The start of a GRB typically depends on the considered energy band (see Figure 8) and some bursts are preceded by a precursor. According to the only BNS merger with a GRB counterpart observed so far [51], the burst will follow around two seconds after the merger. On a time scale of 1000 s this small shift of the time window should have negligible effects. Moreover, a 1000 s time window is conservative in the case of BNS mergers, since the SGRB that follows will typically last a few seconds, as seen in Figure 2. The SGRBs that do show signs of a precursor do so no longer than 2 s before the start of prompt emission. However, the statistics for these events are low, since only a handful of SGRBs with precursors have been observed as of yet [89, 91].

## 4.2 Bayesian logical interference

Consider a hypothesis  $\mathcal{H}$ . Its plausibility is defined as the probability  $P(\mathcal{H}|DI)$  that the hypothesis is correct, given a data set  $D$  and some prior information  $I$ . The prior information should specify how the introduction of a new set of data  $D$  alters the plausibility of  $\mathcal{H}$ . One can relate the posterior plausibility to the plausibility  $P(\mathcal{H}|I)$  prior to obtaining the observational data, by the Bayes theorem

$$P(\mathcal{H}|DI) = P(\mathcal{H}|I) \frac{P(D|\mathcal{H}I)}{P(D|I)}. \quad (33)$$

The probability of obtaining the data set  $D$  given that the hypothesis  $\mathcal{H}$  is true, is given by the so-called likelihood  $P(D|\mathcal{H}I)$  and the global likelihood of obtaining  $D$  is  $P(D|I)$ . Now suppose that two hypotheses  $\mathcal{H}_i$  and  $\mathcal{H}_j$  are mutually exclusive:  $P(\mathcal{H}_i|\mathcal{H}_jI) = 0$ .

The odds ratio  $O_{ij}$  of  $\mathcal{H}_i$  with respect to  $\mathcal{H}_j$  is the relative plausibility between the two hypotheses

$$O_{ij} = \frac{P(\mathcal{H}_i|DI)}{P(\mathcal{H}_j|DI)} = \frac{P(\mathcal{H}_i|I)}{P(\mathcal{H}_j|I)} \frac{P(D|\mathcal{H}_iI)}{P(D|\mathcal{H}_jI)}, \quad (34)$$

where the Bayes theorem is used to arrive at the final expression. This is a useful measure to quantify the plausibility of one hypothesis over another. Now suppose that there are only two possible hypotheses:  $\mathcal{H}$  or  $\bar{\mathcal{H}} = \{\mathcal{H} \text{ is false}\}$ . The odds ratio then expresses the absolute plausibility of  $\mathcal{H}$ , e.g. relative to *any* alternative

$$O(\mathcal{H}|DI) = \frac{P(\mathcal{H}|DI)}{P(\bar{\mathcal{H}}|DI)}. \quad (35)$$

It is convenient to rescale the odds ratio on a logarithmic (decibel) scale and define it as the evidence  $e(\mathcal{H}|DI) = 10 \log_{10}(O(\mathcal{H}|DI))$ . This can be rewritten using Equation (34) into a more suggestive form

$$e(\mathcal{H}|DI) = e(\mathcal{H}|I) + 10 \log_{10} \left( \frac{P(D|\mathcal{H}I)}{P(D|\bar{\mathcal{H}}I)} \right). \quad (36)$$

This reveals that the evidence can be split up in a part that only contains prior information and another part that takes into account the effects of the obtained data. Define the data-dependent parameters  $\psi = -10 \log_{10} P(D|\mathcal{H}I)$  and  $\bar{\psi} = -10 \log_{10} P(D|\bar{\mathcal{H}}I)$ . Interchanging  $\mathcal{H}$  with  $\bar{\mathcal{H}}$  in Equation (36) then results in

$$e(\bar{\mathcal{H}}|DI) = e(\bar{\mathcal{H}}|I) + \psi - \bar{\psi} \leq e(\bar{\mathcal{H}}|I) + \psi. \quad (37)$$

This inequality holds only because  $\bar{\psi} \geq 0$ , since the negative logarithm of a probability between 0 and 1 is always positive. So, given that a data set  $D$  is observed, the evidence to support  $\bar{\mathcal{H}}$  increases by at most  $\psi$  decibels compared to the evidence prior to any observation. Consequently, there is no alternative to  $\mathcal{H}$  which can be supported by more than  $\psi$  decibels, relative to  $\mathcal{H}$  itself. It is useful to take for  $\mathcal{H}$  the background-only hypothesis such that  $\psi$  becomes a measure of the incompatibility of the data with only background.

This method of Bayesian hypothesis testing can be applied to time profile stacking analyses [90]. In particular, we would like to know how likely it is that an on-source distribution of relative neutrino arrival times, like in Figure 18a, is the result of a statistical fluctuation of the background. For this purpose the neutrino events shown in Figure 18a are put into  $n$  bins of equal width  $T_{\text{bin}}$  (see Figure 19a). This allows to determine an explicit formula for  $\psi$  [90]. The probability  $P(m_1 \dots m_n | \mathcal{H}_0 I)$  of distributing  $m$  neutrinos in  $n$  bins with  $m_k$  neutrinos in the  $k$ -th bin is given by the multinomial distribution

$$P(m_1 \dots m_n | \mathcal{H}_0 I) = m! \prod_{k=1}^n \frac{p_k^{m_k}}{m_k!}. \quad (38)$$

Assuming that the background-only hypothesis holds, a neutrino can end up in any of the bins with an equal probability  $p_k = 1/n$ . The expression above fully defines the probability that the data set  $D$  is obtained for the background-only hypothesis.

Thus,  $P(D|\mathcal{H}I)$  can be identified with  $P(m_1\dots m_n|\mathcal{H}_0I)$  and after substituting the values for  $p_k$  one gets

$$\psi = -10 \left[ \log_{10} m! + m \log_{10}(1/n) - \sum_{k=1}^n \log_{10} m_k! \right]. \quad (39)$$

This value is not an absolute measure, it has to be taken relative to the  $\psi$ -value of the background. To achieve this,  $10^4$  pseudo experiments are generated which sample neutrino arrival times from the background distribution. The  $\psi$ -value of each of these experiments is calculated, resulting in a distribution for  $\psi_{\text{bkg}}$  with its own mean value and statistical spread, as shown in Figure 19b. To claim an excess of signal neutrinos from the GRBs, the observed  $\psi$  should be as high as possible compared to the background distribution.

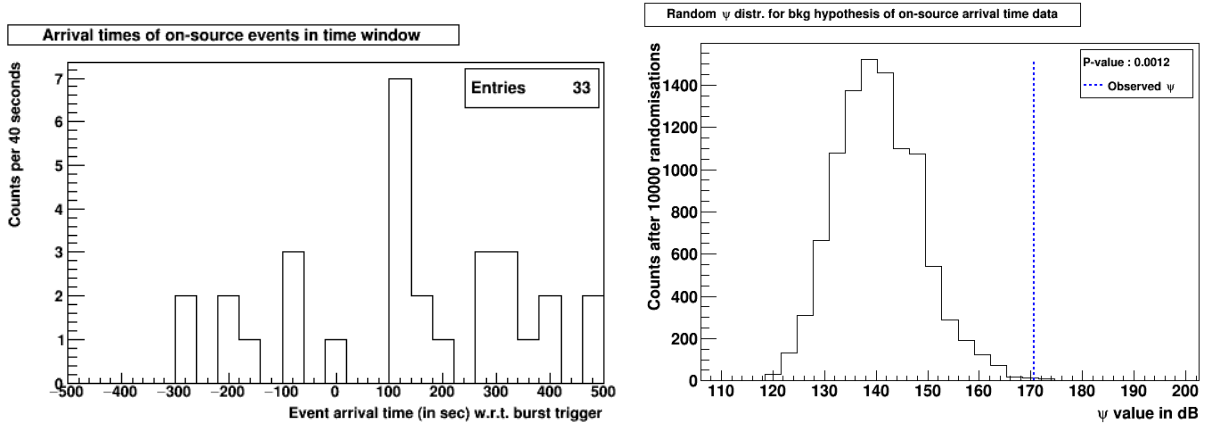


Figure 19: Left: binning of the neutrino arrival times of Figure 18a. Right: the observed  $\psi$  value, presented as the blue dashed line, compared to the  $\psi$  distribution of  $10^4$  randomised background time profiles. The observed  $\psi$  has a p-value of 0.0012 with respect to this distribution, corresponding to  $3.2\sigma$  significance above background levels for a single-sided Gaussian.

## 5 Results of the Toy model

In this section, it will be assumed that a population of BNS mergers is observed by ET solely or by ET and a network of additional interferometers. There will be a one-to-one correspondence between a BNS merger and a SGRB, meaning that every merger will result in a GRB. The goal is to investigate how many bursts are required to observe a neutrino excess with  $5\sigma$  significance, based on the current flux limits. In addition, we can estimate the operation time needed for ET and IceCube to achieve this significance.

### 5.1 Model parameters

First of all, the event selection as described in Section 3.3 still applies. Events that enter the IceCube detector between a declination of  $5^\circ$  and  $85^\circ$  are accepted for analysis. Declinations above  $85^\circ$  are excluded because the on-source and off-source regions can overlap. By only using events from the Northern Hemisphere, the atmospheric muon background is eliminated completely. The downside is that we can only use around half of the potentially observed GRBs, i.e. only those from the Northern Hemisphere. The atmospheric neutrino background rate for this event selection is 3 mHz.

Flux limits on SGRB neutrino emission have been determined by Casier (2015) [92] for 84 SGRBs that were observed during four years of the IC86 run. No statistically significant events have been found, so instead the upper limits on the per-burst fluence are given at 90% confidence level. A Waxman-Bahcall spectrum is assumed with a fluence normalisation  $S_0 = 0.005 \text{ GeV}^{-1} \text{ cm}^{-2}$  for a neutrino break  $\varepsilon_b = 10^6 \text{ GeV}$

$$\frac{dS_\nu}{dE} = S_0(\varepsilon_b) \begin{cases} \varepsilon_b^{-1} E^{-1} & \text{for } E < \varepsilon_b \\ E^{-2} & \text{for } \varepsilon_b < E < 10\varepsilon_b \\ (10\varepsilon_b)^2 E^{-4} & \text{for } E > 10\varepsilon_b \end{cases} \quad (40)$$

These parameters are inserted in Equation (25), where the sum only includes the OneWeights between  $5^\circ$  and  $85^\circ$ . The expected number of detected neutrinos from a burst with this fluence is  $N = 0.034$ . Of course, this is an upper limit, and one GRB can on average result in *at most* this number of detectable neutrinos. It is also assumed that each GRB in the toy model emits all its neutrinos, if any, within the 1000 s time window.

As discussed by Chan (2018) [93], ET will be able to follow GW signals from BNS systems for several days before merging. This allows the interferometer to follow the binary across the sky as the earth rotates and capture the time dependent signal. This signal can be used to estimate the position without the need of triangulation. However, GWs that originate from sources further away do not provide a detectable signal long enough in order to be precisely localised. Around 5% of the BNS mergers up to a distance of 1.6 Gpc will be able to be localised within a  $100 \text{ deg}^2$  patch. However, if a second interferometer is included that can detect the same signals as ET, the accuracy of the localisation can increase dramatically, as shown in Table 1. A network of ET and CE can localise 92% of the sources within  $100 \text{ deg}^2$  up to distances of 1.6 Gpc ( $z = 0.38$ ). Assuming that the source is localised within a circular patch of  $100 \text{ deg}^2$ , the uncertainty on the angular position is  $5.6^\circ$ . As a conservative limit, all neutrinos within  $7^\circ$  of the reconstructed position will be selected for the time profile stacking analysis.

Table 1: The localisation of BNS mergers for several distance ranges  $d$ . The third and fourth column show the upper limit of the 90% credibility regions for the 50% and 90% best localised sources respectively. The fifth and sixth column show the percentage of sources that can be localised within at most  $100 \text{ deg}^2$  and  $30 \text{ deg}^2$  respectively. The number of injected events for the analysis is  $n$ . From Chan (2018) [93].

Network	d (Mpc)	$n$	50% ( $\text{deg}^2$ )	90% ( $\text{deg}^2$ )	$\leq 100$ ( $\text{deg}^2$ )	$\leq 30$ ( $\text{deg}^2$ )
ET	40		2	8	100%	100%
	200		42	183	74%	40%
	400	500	187	837	36%	16%
	800		764	3485	11%	5%
	1600		3994	$1.7 \times 10^4$	5%	2%
	Uniform <sup>1</sup>	3000	$1.7 \times 10^4$	> Sky	3%	2%
CE	40		252	2212	30%	10%
	200		6118	> Sky	1%	0%
	400	500	$2.6 \times 10^4$	> Sky	0%	0%
	800		> Sky	> Sky	0%	0%
	1600		> Sky	> Sky	0%	0%
	Uniform <sup>1</sup>	5000	> Sky	> Sky	0%	0%
ET & CE	40		$2 \times 10^{-2}$	$8 \times 10^{-2}$	100%	100%
	200		$5 \times 10^{-1}$	1.8	100%	100%
	400	500	2	7	100%	99%
	800		7	23	99%	94%
	1600		27	85	92%	55%
	Uniform <sup>1</sup>	5000	128	538	41%	12%

<sup>1</sup>Uniformly distributed in the comoving volume.

The average time difference  $\mu_\tau$  between the time of merger  $t_0$  and the neutrino emission will be 2 s, corresponding to the observed delay of GRB 170817. In principle this parameter should have no effect on the outcome of the experiment, as long as it lies at least  $3\sigma_\tau$  from the edges of the time window. The statistical spread  $\sigma_\tau$  on the time difference has a more noticeable effect. Obviously, if the spread is very small, most signal neutrinos will end up in the same bin. In the view of the background-only hypothesis, this is rather unlikely and statistical significance will be higher. In reality, it would be reasonable to assume that most of the prompt neutrino emission will arrive during the GRB, which typically lasts a few seconds. Still, the possibility remains that extended emission takes place, so the spread is taken to be  $\sigma_\tau = 10 \text{ s}$ .

The bin size of the time profiles should be around the same size as the temporal spread of the neutrino arrival times, such that most of the signal neutrinos end up in the same bin. In reality, the signal+background PDF of the relative neutrino arrival time  $\tau$  is known, but the signal-only PDF is not. So the spread  $\sigma_\tau$  will appear wider and will be overestimated because of the background events. We will take a conservative limit of  $T_{\text{bin}} = 5\sigma_\tau$ , corresponding to 50 s.

## 5.2 Interpretation of results

For a fixed spread  $\sigma_\tau$  on the neutrino arrival time, the number of bursts is increased until a neutrino excess of at least  $5\sigma$  significance is achieved. This corresponds to a p-value of  $5 \times 10^{-7}$  for a single-sided Gaussian. Again, the  $\psi$ -value of the neutrinos population in the on-source time window will be calculated and compared to the background distribution. Since the background distribution for  $\psi_{\text{bkg}}$  is constructed by randomised pseudo-experiments, we need  $\sim 10^7$  randomisations in order to obtain a PDF that is accurate enough to calculate such a p-value. To keep the computation time reasonable, the number of randomised pseudo-experiments is capped at  $4 \times 10^7$ .

ET on its own will be able to detect around  $7 \times 10^4$  BNS mergers per year, as mentioned before. Unfortunately, only a fraction of these events can be localised well enough in order to be suitable for time profile stacking. So we will limit ourselves to the BNS mergers that can be localised within a patch of  $100 \text{ deg}^2$ . For ET this is 5% of the mergers up to 1.6 Gpc. The BNS merger rate per unit volume  $R_m$  at this distance is roughly the same as in the local universe ( $R_m(z = 0)$ ). The GW signals of BNS mergers that are observed so far give a rough estimate of this local merger rate. The results do depend on the assumed mass distribution of neutron stars, which is considered to be either flat or Gaussian. The merger rate densities inferred from the two first observation runs (*O1* & *O2*) of LIGO/Virgo are

$$R_m(z = 0) = 662_{-565}^{+1609} \text{ Gpc}^{-3} \text{ yr}^{-1} \quad (41)$$

for a flat mass distribution and

$$R_m(z = 0) = 920_{-790}^{+2220} \text{ Gpc}^{-3} \text{ yr}^{-1} \quad (42)$$

for a Gaussian mass distribution [94]. The uncertainties on  $R_m$  are the 90% confidence intervals, which are quite large because of the limited amount of BNS mergers observed during *O1* and *O2*. They nonetheless seem to be consistent with earlier studies based on the currently known population of binary pulsars [95–97]. Still, these values will have to be revised in the future, when more data is available.

Based on these numbers, the merger rate within 1.6 Gpc becomes  $1.14 \times 10^4 \text{ yr}^{-1}$  and  $1.58 \times 10^4 \text{ yr}^{-1}$ , for flat and Gaussian mass distributions respectively. With ET, 5% of these mergers can be localised within  $100 \text{ deg}^2$ , of which roughly half are accepted for our analysis since we only look at one hemisphere. So the merger rates that are relevant for the multi-messenger analysis are

$$r_m(\leq 1.6 \text{ Gpc}) = 0.5 \cdot 0.05 \begin{cases} 1.14 \times 10^4 \text{ yr}^{-1} = 283 \text{ yr}^{-1} \\ 1.58 \times 10^4 \text{ yr}^{-1} = 395 \text{ yr}^{-1} \end{cases} \quad (43)$$

again for a flat and Gaussian mass distribution respectively. These results are in good agreement with a more detailed study [98], of which the result is shown in Figure 20.

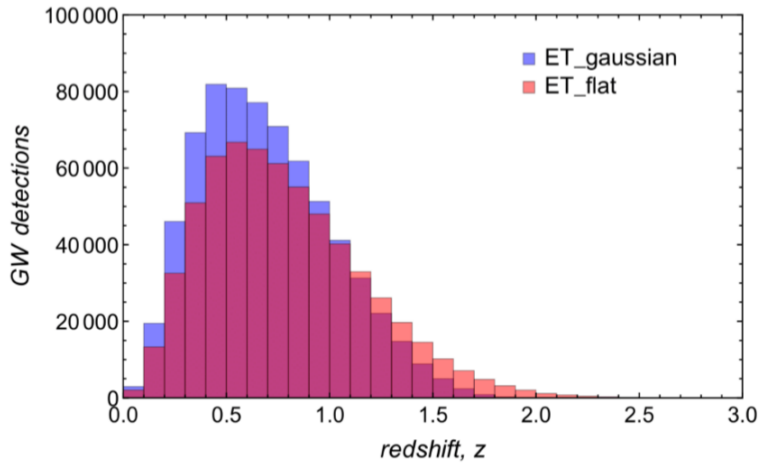


Figure 20: The expected redshift distribution of BNS detections by ET for eight years of operation time. A distance of 1.6 Gpc corresponds to a redshift of 0.38. From Belgacem (2019) [98].

For a temporal spread  $\sigma_\tau = 10$  s, the median number of GRBs required is 895, in order to achieve  $5\sigma$  exclusion of the background-only hypothesis, as shown in Figure 22. This means that, if all GRBs emit at exactly the current flux limit, it will take ET and IceCube 2.27 – 3.15 yr to find a signal at  $5\sigma$  significance, depending on the assumed NS mass distribution. In our toy model, a total of 45 neutrinos (signal+background) have been found in the on-source time window, compared to 19 in the off-source time window which should contain only background (see Figure 21). It is most likely that the actual neutrino flux of a BNS merger lies below the current limit and IceCube will not record this amount of neutrinos. In this case, any additional ET+IceCube observation time can be used to put a more stringent limit on the neutrino flux. Note that the current flux limit is calculated at 90% confidence. With the multi-messenger analysis described above, the same upper limit can be set at  $5\sigma$  significance, after 2.27 – 3.15 yr of observation time.

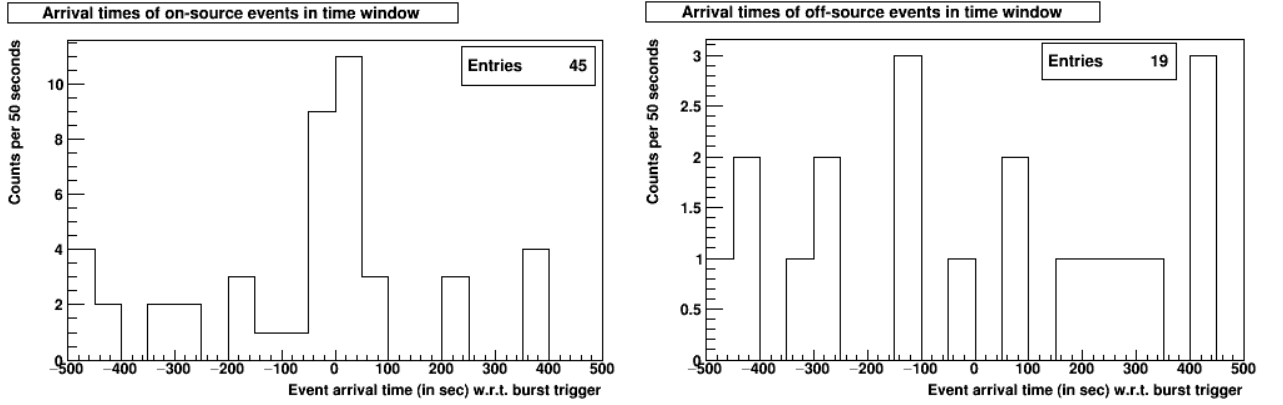


Figure 21: Left: the stacked arrival times of neutrinos within a  $7^\circ$  opening angle of the burst positions and a signal spread  $\sigma_\tau = 10$  s. Right: the stacked arrival times of background neutrinos in the corresponding off-source time windows.

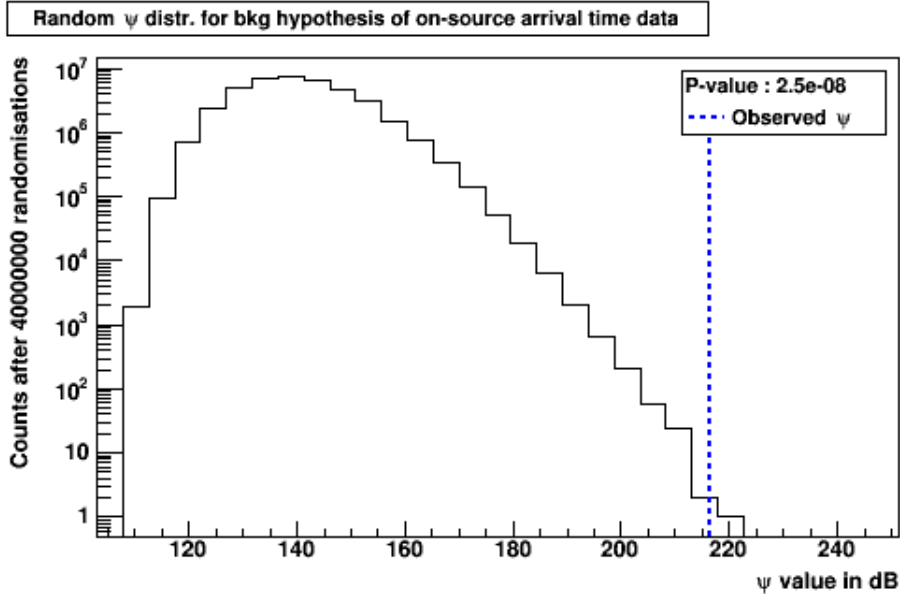


Figure 22: The  $\psi$ -value of the observed collection of neutrinos in the on-source time window, compared to the background  $\psi$  distribution.

A network of ET and CE will have a significantly larger potential, since it will be able to localise 92% of the sources within a  $100 \text{ deg}^2$  at the same distance, compared to 5% for ET alone. The rate of events that can be used for time profile stacking increases to  $5244 - 7268 \text{ yr}^{-1}$  for an ET+CE+IceCube network. For a rate this high,  $5\sigma$  significance can be reached after just  $0.12 - 0.17 \text{ yr}$ . The results are summarised in Table 2, together with the error ranges induced by the merger rate densities. It can be seen that in a worst-case scenario, if the merger rate density ends up being at the lower end of the 90% confidence interval, it can take ET several decades to obtain the desired results. However, if CE is included then this will take barely over one year, even in the worst case.

Table 2: The observation time needed for ET or ET+CE to obtain  $5\sigma$  significance. The 90% confidence intervals are taken from Equation (41) and (42) and are translated into the corresponding intervals for the observation times. The left number in each cell represents the observation time for a Gaussian mass distribution and the right number for a flat mass distribution.

Observation time	ET (yr)	ET + CE (yr)
Lower 90%	16.05 - 21.51	0.87 - 1.17
Central value	2.27 - 3.15	0.12 - 0.17
Upper 90%	0.67 - 0.92	0.04 - 0.05

## 6 Conclusion and outlook

The combination of gravitational wave and neutrino astronomy presents a powerful tool for studying short-duration GRBs, which are thought to be caused mainly by neutron star mergers. Where the current GW observatories have only been able to detect a handful of BNS merger candidates, the next-generation Einstein Telescope is predicted to observe several thousand mergers per year. Currently, IceCube has not yet identified a significant neutrino signal from (short) GRBs. Using the resulting current upper-limits on the maximally allowed neutrino flux from short GRBs and assuming a one-to-one correspondence between short GRBs and BNS mergers, we used a toy model to study the prospects of observing neutrinos in coincidence with BNS mergers. With these assumptions, IceCube could potentially be able to detect up to around 25 neutrinos from roughly 900 neutron star mergers localised by Einstein Telescope. With the time profile stacking analysis, this neutrino excess can confirm the existence of correlated neutrino production with  $5\sigma$  significance within 2.3 to 3.2 years of ET and IceCube operation, or otherwise provide more stringent flux limits. It is also shown that a network with an additional GW observatory, like the Cosmic Explorer, could do the same in just two months. At this rate, one can hope to quickly build up a catalog of GRB neutrino candidates. In turn, these neutrinos can be related to the underlying proton spectrum of the GRB and the physics involved in their acceleration.

These results are based entirely upon localisation by gravitational waves, for sources within an uncertainty region of  $100 \text{ deg}^2$  and closer than 1.6 Gpc. Part of these mergers will be able to be localised within a significantly smaller region, further reducing background. Additionally, a fraction of the merger population will most likely result in a detectable GRB and possibly an afterglow, which can be used for very precise localisation. It should be noted as well that the same method can be applied to NS-BH mergers, although the expected number of mergers of this type is relatively small.

As an outlook to further studies, it is worth mentioning that IceCube is planned to undergo an upgrade towards IceCube-Gen2 [99, 100]. This extension of IceCube with a  $10 \text{ km}^3$  detector volume will greatly increase the potential for detecting neutrinos with energies above 1 PeV. For a multi-messenger study involving IceCube-Gen2, the effective area for detecting neutrinos has to be re-evaluated accordingly, enhancing the detection rate. Furthermore, as long as the current GW observatories keep gathering data, the BNS merger rate in the local universe can be determined more accurately. Since the uncertainties in this study are dominated by the uncertainty on these merger rates, an update on these values has the potential to drastically influence the numerical results presented here.

## References

- [1] R.W. Klebesadel, I.B. Strong, and R.A. Olson. Observations of gamma-ray bursts of cosmic origin. *The Astrophysical Journal*, 182, 1973.
- [2] Wm. A. Wheaton, M.P. Ulmer, W.A. Baity, D.W. Datlowe, M.J. Elcan, L.E. Peterson, R.W. Klebesadel, I.B. Strong, T.L. Cline, and U.D. Desai. The direction and spectral variability of a cosmic gamma-ray burst. *The Astrophysical Journal*, 185:L57, Oct 1973.
- [3] A. von Kienlin, C. A. Meegan, W. S. Paciesas, P. N. Bhat, E. Bissaldi, M. S. Briggs, E. Burns, W. H. Cleveland, M. H. Gibby, M. M. Giles, A. Goldstein, R. Hamburg, C. M. Hui, D. Kocevski, B. Mailyan, C. Malacaria, S. Poolakkil, R. D. Preece, O. J. Roberts, P. Veres, and C. A. Wilson-Hodge. The Fourth Fermi-GBM Gamma-Ray Burst Catalog: A Decade of Data. *The Astrophysical Journal*, 893(1):46, April 2020.
- [4] V. Schoenfelder, H. Aarts, K. Bennett, H. de Boer, J. Clear, W. Collmar, A. Connors, A.J.M. Deerenberg, R. Diehl, A. von Dordrecht, et al. Instrument description and performance of the imaging gamma-ray telescope COMPTEL aboard the Compton Gamma-Ray Observatory. *Astrophysical Journal Supplement Series*, 86:657, 1993.
- [5] G.J. Fishman, C.A. Meegan, R.B. Wilson, W.S. Paciesas, T.A. Parnell, R.W. Austin, J.R. Rehage, and J.L. Matteson. BATSE: The burst and transient source experiment on the gamma ray observatory. In *Proc. GRO Science Workshop, GSFC*, volume 2, 1989.
- [6] C.A. Meegan, G.J. Fishman, R.B. Wilson, W.S. Paciesas, G.N. Pendleton, J.M. Horack, M.N. Brock, and C. Kouveliotou. Spatial distribution of  $\gamma$ -ray bursts observed by BATSE. *Nature*, 355(6356):143–145, 1992.
- [7] Boella, G., Butler, R.C., Perola, G.C., Piro, L., Scarsi, L., and Bleeker, J.A.M. BeppoSAX, the wide band mission for X-ray astronomy. *Astron. Astrophys. Suppl. Ser.*, 122(2):299–307, 1997.
- [8] T. Galama J. van Paradijs, P.J. Groot. Transient optical emission from the error box of the  $\gamma$ -ray burst of 28 february 1997. *Nature*, 386:686–689, April 1997.
- [9] D.E. Reichart. The redshift of GRB 970508. *The Astrophysical Journal*, 495(2):L99–L101, March 1998.
- [10] M.R. Metzger, S.G. Djorgovski, S.R. Kulkarni, C.C. Steidel, K.L. Adelberger, D.A. Frail, E. Costa, and F. Frontera. Spectral constraints on the redshift of the optical counterpart to the  $\gamma$ -ray burst of 8 May 1997. *Nature*, 387(6636):878–880, 1997.
- [11] B. Gendre, G. Stratta, J.L. Atteia, S. Basa, M. Bor, D.M. Coward, S. Cutini, V. DElia, E.J. Howell, A. Klotz, et al. The ultra-long gamma-ray burst 111209A: The collapse of a blue supergiant? *The Astrophysical Journal*, 766(1):30, Mar 2013.
- [12] B. Zhang, B. Zhang, K. Murase, V. Connaughton, and M. S. Briggs. How long does a burst burst? *The Astrophysical Journal*, 787(1):66, May 2014.
- [13] S.E. Woosley and J.S. Bloom. The supernovagamma-ray burst connection. *Annual Review of Astronomy and Astrophysics*, 44(1):507556, Sep 2006.
- [14] J.S. Bloom, J.X. Prochaska, D. Pooley, et al. Closing in on a shorthard burst progenitor: Constraints from earlytime optical imaging and spectroscopy of a possible host galaxy of GRB 050509b. *The Astrophysical Journal*, 638(1):354368, Feb 2006.
- [15] J.X. Prochaska, J.S. Bloom, H.W. Chen, et al. The galaxy hosts and largescale environments of shorthard gammaray bursts. *The Astrophysical Journal*, 642(2):989994, May 2006.
- [16] T. Piran. Gamma-ray bursts and the fireball model. *Physics Reports*, 314(6):575667, Jun 1999.

- [17] T. Piran. The physics of gamma-ray bursts. *Reviews of Modern Physics*, 76(4):11431210, Jan 2005.
- [18] P. Mészáros. The fireball model of gamma-ray bursts. *Progress of Theoretical Physics Supplement*, 143:33–49, 2001.
- [19] S. Razzaque. Synchrotron radiation from ultra-high energy protons and the Fermi observations of GRB 080916C. *The Open Astronomy Journal*, 3(1):150155, Aug 2010.
- [20] M.G. Baring. High-energy spectral signatures in gamma-ray bursts. *AIP Conference Proceedings*, 2000.
- [21] K. Murase and K. Ioka. Closure relations fore±pair signatures in gamma-ray bursts. *The Astrophysical Journal*, 676(2):1123–1129, apr 2008.
- [22] B. Zhang. *The physics of gamma-ray bursts*. Cambridge University Press, 2019.
- [23] D. Perkins. *Particle Astrophysics*. Oxford University Press, 2009.
- [24] D.A. Frail, S.R. Kulkarni, R. Sari, S.G. Djorgovski, J.S. Bloom, T.J. Galama, D.E. Reichart, E. Berger, F.A. Harrison, P.A. Price, et al. Beaming in gamma-ray bursts: Evidence for a standard energy reservoir. *The Astrophysical Journal*, 562(1):L55L58, Nov 2001.
- [25] A. Gomboc. Unveiling the secrets of gamma ray bursts. *Contemporary Physics*, 53(4):339355, Jul 2012.
- [26] E. Waxman. Cosmological gamma-ray bursts and the highest energy cosmic rays. *Physical Review Letters*, 75(3):386389, Jul 1995.
- [27] P. Mészáros. Gamma-ray bursts. *Reports on Progress in Physics*, 69(8):22592321, Jul 2006.
- [28] J.P. Rachen and P. Mszros. Photohadronic neutrinos from transients in astrophysical sources. *Physical Review D*, 58(12), Nov 1998.
- [29] A. Achterberg, Y.A. Gallant, J.G. Kirk, and A.W. Guthmann. Particle acceleration by ultrarelativistic shocks: theory and simulations. *Monthly Notices of the Royal Astronomical Society*, 328(2):393408, Dec 2001.
- [30] D. Band, J. Matteson, L. Ford, B. Schaefer, D. Palmer, B. Teegarden, T. Cline, M. Briggs, W. Paciesas, G. Pendleton, G. Fishman, C. Kouveliotou, C. Meegan, R. Wilson, and P. Lestrade. BATSE observations of gamma-ray burst spectra. I. spectral diversity. *The Astrophysical Journal*, 413:281, August 1993.
- [31] B.-B. Zhang, Z.L. Uhm, V. Connaughton, M.S. Briggs, and B. Zhang. Synchrotron origin of the typical GRB band functiona case study of GRB 130606B. *The Astrophysical Journal*, 816(2):72, Jan 2016.
- [32] S. Razzaque, P. Mészáros, and E. Waxman. Neutrino tomography of gamma ray bursts and massive stellar collapses. *Physical Review D*, 68(8), Oct 2003.
- [33] E. Waxman and J. Bahcall. High energy neutrinos from cosmological gamma-ray burst fireballs. *Physical Review Letters*, 78(12):22922295, Mar 1997.
- [34] E. Waxman and J. Bahcall. High energy neutrinos from astrophysical sources: An upper bound. *Physical Review D*, 59(2), Dec 1998.
- [35] A. Einstein. Näherungsweise Integration der Feldgleichungen der Gravitation. *Sitzungsberichte der Königlich Preußischen Akademie der Wissenschaften (Berlin)*, pages 688–696, January 1916.
- [36] S. Carroll. *Spacetime and geometry, an introduction to general relativity*. Pearson education limited, 2014.

- [37] Y. Sekiguchi and M. Shibata. Axisymmetric collapse simulations of rotating massive stellar cores in full general relativity: Numerical study for prompt black hole formation. *Physical Review D*, 71(8), Apr 2005.
- [38] H. Dimmelmeier, C.D. Ott, A. Marek, and H.-T. Janka. Gravitational wave burst signal from core collapse of rotating stars. *Physical Review D*, 78(6), Sep 2008.
- [39] C.D. Ott, E.P. OConnor, S. Gossan, E. Abdikamalov, U.C.T. Gamma, and S. Drasco. Core-collapse supernovae, neutrinos, and gravitational waves. *Nuclear Physics B - Proceedings Supplements*, 235-236:381387, Feb 2013.
- [40] S.W. Barwick, J.F. Beacom, V. Cianciolo, S. Dodelson, J.L. Feng, G.M. Fuller, M. Kaplinghat, D.W. McKay, P. Meszaros, A. Mezzacappa, H. Murayama, K.A. Olive, T. Stanev, and T.P. Walker. APS neutrino study: Report of the neutrino astrophysics and cosmology working group, 2004.
- [41] K. Scholberg. Supernova neutrino detection. *Annual Review of Nuclear and Particle Science*, 62(1):81103, Nov 2012.
- [42] J. Cervantes-Cota, S. Galindo-Uribarri, and G. Smoot. A brief history of gravitational waves. *Universe*, 2(3):22, Sep 2016.
- [43] Y. Hagihara, N. Era, D. Iikawa, N. Takeda, and H. Asada. Condition for directly testing scalar modes of gravitational waves by four detectors. *Physical Review D*, 101(4), Feb 2020.
- [44] D.V. Martynov, E.D. Hall, B.P. Abbott, R. Abbott, T.D. Abbott, C. Adams, R.X. Adhikari, R.A. Anderson, S.B. Anderson, K. Arai, et al. Sensitivity of the advanced ligo detectors at the beginning of gravitational wave astronomy. *Physical Review D*, 93(11), Jun 2016.
- [45] B.P. Abbott, R. Abbott, T.D. Abbott, F. Acernese, K. Ackley, C. Adams, T. Adams, P. Addesso, R.X. Adhikari, V.B. Adya, et al. Gravitational waves and gamma-rays from a binary neutron star merger: GW170817 and GRB 170817A. *The Astrophysical Journal*, 848(2):L13, Oct 2017.
- [46] B.P. Abbott, R. Abbott, R. Adhikari, P. Ajith, B. Allen, G. Allen, R.S. Amin, S.B. Anderson, W.G. Anderson, M.A. Arain, et al. LIGO: the laser interferometer gravitational-wave observatory. *Reports on Progress in Physics*, 72(7):076901, Jun 2009.
- [47] T. Accadia, F. Acernese, M. Alshourbagy, and P. Amico. Virgo: a laser interferometer to detect gravitational waves. *Journal of Instrumentation*, 7(03):P03012–P03012, mar 2012.
- [48] F. Acernese, M. Agathos, K. Agatsuma, D. Aisa, N. Allemandou, A. Allocca, J. Amarni, P. Astone, G. Balestri, G. Ballardin, et al. Advanced virgo: a second-generation interferometric gravitational wave detector. *Classical and Quantum Gravity*, 32(2):024001, Dec 2014.
- [49] H. Lück, C. Affeldt, J. Degallaix, A. Freise, H. Grote, M. Hewitson, S. Hild, J. Leong, M. Prijatelj, K.A. Strain, et al. The upgrade of GEO 600. *Journal of Physics: Conference Series*, 228:012012, May 2010.
- [50] T. Akutsu, M. Ando, K. Arai, Y. Arai, S. Araki, A. Araya, N. Aritomi, H. Asada, Y. Aso, S. Atsuta, K. Awai, S. Bae, L. Baiotti, M. Barton, K. Cannon, E. Capocasa, C.-S. Chen, T.-W. Chiu, and K. Cho. KAGRA: 2.5 generation interferometric gravitational wave detector. *Nature Astronomy*, 3:35–40, Jan 2019.
- [51] B.P. Abbott, R. Abbott, T.D. Abbott, F. Acernese, K. Ackley, C. Adams, T. Adams, P. Addesso, R.X. Adhikari, V.B. Adya, et al. GW170817: Observation of gravitational waves from a binary neutron star inspiral. *Physical Review Letters*, 119(16), Oct 2017.
- [52] F. Özel, D. Psaltis, R. Narayan, and A. Santos Villarreal. On the mass distribution and birth masses of neutron stars. *The Astrophysical Journal*, 757(1):55, Sep 2012.

- [53] D.A. Coulter, R.J. Foley, C.D. Kilpatrick, M.R. Drout, A.L. Piro, B.J. Shappee, M.R. Siebert, J.D. Simon, N. Ulloa, D. Kasen, et al. Swope supernova survey 2017a (SSS17a), the optical counterpart to a gravitational wave source. *Science*, 358(6370):15561558, Oct 2017.
- [54] B.P. Abbott, R. Abbott, T.D. Abbott, F. Acernese, K. Ackley, C. Adams, T. Adams, P. Addesso, R.X. Adhikari, V.B. Adya, et al. Multi-messenger observations of a binary neutron star merger. *The Astrophysical Journal*, 848(2):L12, Oct 2017.
- [55] E. Troja, L. Piro, H. van Eerten, R.T. Wollaeger, M. Im, O.D. Fox, N.R. Butler, S.B. Cenko, T. Sakamoto, C.L. Fryer, et al. The X-ray counterpart to the gravitational-wave event GW170817. *Nature*, 551(7678):7174, Oct 2017.
- [56] G. Hallinan, A. Corsi, K.P. Mooley, K. Hotokezaka, E. Nakar, M.M. Kasliwal, D.L. Kaplan, D.A. Frail, S.T. Myers, T. Murphy, et al. A radio counterpart to a neutron star merger. *Science*, 358(6370):15791583, Oct 2017.
- [57] B.D. Metzger. Kilonovae. *Living Reviews in Relativity*, 20(1), May 2017.
- [58] S. Valenti, J.S. David, S. Yang, E. Cappellaro, L. Tartaglia, A. Corsi, S.W. Jha, D.E. Reichart, J. Haislip, and V. Kouprianov. The discovery of the electromagnetic counterpart of GW170817: Kilonova AT 2017gfo/DLT17ck. *The Astrophysical Journal*, 848(2):L24, oct 2017.
- [59] E. Pian, P. D'Avanzo, S. Benetti, M. Branchesi, E. Brocato, S. Campana, E. Cappellaro, S. Covino, V. DElia, J.P.U. Fynbo, et al. Spectroscopic identification of r-process nucleosynthesis in a double neutron-star merger. *Nature*, 551(7678):6770, Oct 2017.
- [60] D. Kasen, B. Metzger, J. Barnes, E. Quataert, and E. Ramirez-Ruiz. Origin of the heavy elements in binary neutron-star mergers from a gravitational-wave event. *Nature*, 551(7678):8084, Oct 2017.
- [61] A. Albert, M. Andr, M. Anghinolfi, M. Ardid, J.J. Aubert, J. Aublin, T. Avgitas, B. Baret, J. Barrios-Mart, S. Basa, et al. Search for high-energy neutrinos from binary neutron star merger GW170817 with ANTARES, IceCube, and the Pierre Auger Observatory. *The Astrophysical Journal*, 850(2):L35, Nov 2017.
- [62] C. Cutler and É.E. Flanagan. Gravitational waves from merging compact binaries: How accurately can one extract the binaries parameters from the inspiral waveform? *Physical Review D*, 49(6):26582697, Mar 1994.
- [63] S.A. Hughes, Szabolcs M., P.L. Bender, and C.J. Hogan. New physics and astronomy with the new gravitational-wave observatories, 2001.
- [64] M. Maggiore, C. Van Den Broeck, N. Bartolo, E. Belgacem, D. Bertacca, M.A. Bizouard, M. Branchesi, S. Clesse, S. Foffa, J. Garca-Bellido, et al. Science case for the Einstein telescope. *Journal of Cosmology and Astroparticle Physics*, 2020(03):050050, Mar 2020.
- [65] B.S. Sathyaprakash and B.F. Schutz. Physics, astrophysics and cosmology with gravitational waves. *Living Reviews in Relativity*, 12(1), Mar 2009.
- [66] T. Regimbau, T. Dent, W. Del Pozzo, S. Giampanis, T.G.F. Li, C. Robinson, C. Van Den Broeck, D. Meacher, C. Rodriguez, B.S. Sathyaprakash, et al. Mock data challenge for the Einstein gravitational-wave telescope. *Physical Review D*, 86(12), Dec 2012.
- [67] F. Badaracco J. Harms. Optimization of seismometer arrays for the cancellation of newtonian noise from seismic body waves, 2019.
- [68] M. Abernathy, F. Acernese, P. Ajith, B. Allen, P. Amaro Seoane, N. Andersson, S. Aoudia, P. Astone, B. Krishnan, L. Barack, et al. Einstein gravitational wave telescope conceptual design study. 2011.

- [69] S. Hild, M. Abernathy, F. Acernese, P. Amaro-Seoane, N. Andersson, K. Arun, F. Barone, B. Barr, M. Barsuglia, M. Beker, et al. Sensitivity studies for third-generation gravitational wave observatories. *Classical and Quantum Gravity*, 28(9):094013, Apr 2011.
- [70] R. OShaughnessy, V. Kalogera, and K. Belczynski. Binary compact object coalescence rates: The role of elliptical galaxies. *The Astrophysical Journal*, 716(1):615633, May 2010.
- [71] E. Belgacem, Y. Dirian, S. Foffa, E.J. Howell, M. Maggiore, and T. Regimbau. Cosmology and dark energy from joint gravitational wave-GRB observations. *Journal of Cosmology and Astroparticle Physics*, 2019(08):015015, Aug 2019.
- [72] J. Miller, L. Barsotti, S. Vitale, P. Fritschel, M. Evans, and D. Sigg. Prospects for doubling the range of Advanced LIGO. *Physical Review D*, 91(6), Mar 2015.
- [73] D. Reitze, R.X. Adhikari, S. Ballmer, B. Barish, L. Barsotti, G. Billingsley, D.A. Brown, Y. Chen, D. Coyne, R. Eisenstein, M. Evans, P. Fritschel, E.D. Hall, A. Lazzarini, G. Lovelace, J. Read, B.S. Sathyaprakash, D. Shoemaker, J. Smith, C. Torrie, S. Vitale, R. Weiss, C. Wipf, and M. Zucker. Cosmic Explorer: The U.S. contribution to gravitational-wave astronomy beyond LIGO, 2019.
- [74] IceCube website. <https://icecube.wisc.edu/>. Accessed: 17-4-2020.
- [75] M.G. Aartsen, M. Ackermann, J. Adams, J.A. Aguilar, M. Ahlers, M. Ahrens, D. Altmann, K. Andeen, T. Anderson, I. Anseau, et al. The IceCube neutrino observatory: instrumentation and online systems. *Journal of Instrumentation*, 12(03):P03012P03012, Mar 2017.
- [76] F. Halzen and S.R. Klein. Invited review article: IceCube: an instrument for neutrino astronomy. *Review of Scientific Instruments*, 81(8):081101, 2010.
- [77] R. Abbasi, Y. Abdou, T. Abu-Zayyad, M. Ackermann, J. Adams, J.A. Aguilar, M. Ahlers, M.M. Allen, D. Altmann, K. Andeen, et al. The design and performance of icecube DeepCore. *Astroparticle Physics*, 35(10):615624, May 2012.
- [78] R. Abbasi, Y. Abdou, M. Ackermann, J. Adams, J.A. Aguilar, M. Ahlers, D. Altmann, K. Andeen, J. Auffenberg, X. Bai, et al. IceTop: The surface component of IceCube. *Nuclear Instruments and Methods in Physics Research Section A: Accelerators, Spectrometers, Detectors and Associated Equipment*, 700:188220, Feb 2013.
- [79] D. Soldin. Recent results of cosmic ray measurements from IceCube and IceTop, 2019.
- [80] J. Ahrens, X. Bai, R. Bay, S.W. Barwick, T. Becka, J.K. Becker, K.H. Becker, E. Bernardini, D. Bertrand, A. Biron, et al. Muon track reconstruction and data selection techniques in CAMANDA. *Nuclear Instruments and Methods in Physics Research Section A: Accelerators, Spectrometers, Detectors and Associated Equipment*, 524(1-3):169194, May 2004.
- [81] A. Bellerive. Review of solar neutrino experiments. *International Journal of Modern Physics A*, 19(08):11671179, Mar 2004.
- [82] J.N. Bahcall, A.M. Serenelli, and S. Basu. New solar opacities, abundances, helioseismology, and neutrino fluxes. *The Astrophysical Journal*, 621(1):L85L88, Jan 2005.
- [83] K.J. Meagher. *Limits on Neutrino Emission from Gamma-Ray Bursts with the 40 String IceCube Detector*. PhD thesis, 2012.
- [84] M.G. Aartsen, K. Abraham, M. Ackermann, J. Adams, J. A. Aguilar, M. Ahlers, M. Ahrens, D. Altmann, K. Andeen, T. Anderson, et al. Observation and characterization of a cosmic muon neutrino flux from the northern hemisphere using six years of IceCube data. *The Astrophysical Journal*, 833(1):3, Dec 2016.
- [85] J. Stettner. Measurement of the diffuse astrophysical muon-neutrino spectrum with ten years of IceCube data, 2019.

- [86] M.G. Aartsen, M. Ackermann, J. Adams, J.A. Aguilar, M. Ahlers, M. Ahrens, D. Altmann, K. Andeen, T. Anderson, I. Ansseau, et al. Astrophysical neutrinos and cosmic rays observed by IceCube. *Advances in Space Research*, 62(10):29022930, Nov 2018.
- [87] Internal documentation of the icecube collaboration.
- [88] N. van Eijndhoven. class NcAstrolab: public TTask, public NcTimestamp. <https://nick-ve.github.io/ncfs/docs/NcAstrolab.html#NcAstrolab:NcAstrolab@1>. accessed: 24-4-2020.
- [89] P. Coppin, K.D. de Vries, and N. van Eijndhoven. Identification of GRB precursors in Fermi-GBM bursts, 2020.
- [90] N. van Eijndhoven. On the observability of high-energy neutrinos from gamma ray bursts. *Astroparticle Physics*, 28(6):540546, Jan 2008.
- [91] S.-Q. Zhong, Z.-G. Dai, J.-G. Cheng, L. Lan, and H.-M. Zhang. Precursors in short gamma-ray bursts as a possible probe of progenitors. *The Astrophysical Journal*, 884(1):25, Oct 2019.
- [92] M. Casier. *Search for High-Energy Neutrino Production in Short Gamma Ray Bursts with the IceCube Neutrino Observatory*. PhD thesis, Brussels U., IIHE, 2015.
- [93] M.L. Chan, C. Messenger, I.S. Heng, and M. Hendry. Binary neutron star mergers and third generation detectors: Localization and early warning. *Physical Review D*, 97(12), Jun 2018.
- [94] B.P. Abbott, R. Abbott, T.D. Abbott, S. Abraham, F. Acernese, K. Ackley, C. Adams, R.X. Adhikari, V.B. Adya, C. Affeldt, et al. GWTC-1: A gravitational-wave transient catalog of compact binary mergers observed by LIGO and Virgo during the first and second observing runs. *Physical Review X*, 9(3), Sep 2019.
- [95] N. Pol, M. McLaughlin, and D.R. Lorimer. Future prospects for ground-based gravitational-wave detectors: The galactic double neutron star merger rate revisited. *The Astrophysical Journal*, 870(2):71, Jan 2019.
- [96] C. Kim, B.B.P. Perera, and M.A. McLaughlin. Implications of PSR J0737-3039B for the galactic NS-NS binary merger rate. *Monthly Notices of the Royal Astronomical Society*, 448(1):928938, Feb 2015.
- [97] M. Burgay, N. D'Amico, A. Possenti, R.N. Manchester, A.G. Lyne, B.C. Joshi, M.A. McLaughlin, M. Kramer, J.M. Sarkissian, F. Camilo, et al. An increased estimate of the merger rate of double neutron stars from observations of a highly relativistic system. *Nature*, 426(6966):531533, Dec 2003.
- [98] E. Belgacem, Y. Dirian, S. Foffa, E.J. Howell, M. Maggiore, and T. Regimbau. Cosmology and dark energy from joint gravitational wave-GRB observations. *Journal of Cosmology and Astroparticle Physics*, 2019(08):015015, Aug 2019.
- [99] IceCube-Gen2 Collaboration. IceCube-Gen2: A vision for the future of neutrino astronomy in Antarctica, 2014.
- [100] M.G. Aartsen, M. Ackermann, J. Adams, J.A. Aguilar, M. Ahlers, M. Ahrens, C. Alispach, K. Andeen, T. Anderson, I. Ansseau, G. Anton, et al. Neutrino astronomy with the next generation IceCube neutrino observatory, 2019.